

Journal of Geophysical Research: Oceans

RESEARCH ARTICLE

10.1002/2014JC010463

Key Points:

- Southern Ocean and tropical Indo-Pacific drive natural variability
- Decadal variability comes from convective events along the Antarctic shelf
- Interannual variability arises from SAM and ENSO climate modes

Supporting Information:

- Readme
- Supplementary_All

Correspondence to:L. Resplandy,
lresplandy@ucsd.edu**Citation:**

Resplandy, L., R. Séférian, and L. Bopp (2015), Natural variability of CO₂ and O₂ fluxes: What can we learn from centuries-long climate models simulations?, *J. Geophys. Res. Oceans*, 120, 384–404, doi:10.1002/2014JC010463.

Received 3 OCT 2014

Accepted 17 DEC 2014

Accepted article online 23 DEC 2014

Published online 28 JAN 2015

Natural variability of CO₂ and O₂ fluxes: What can we learn from centuries-long climate models simulations?

L. Resplandy^{1,2}, R. Séférian³, and L. Bopp¹

¹Laboratory for Science of Climate and Environment, IPSL, CEA-UVSQ-CNRS, Gif-sur-Yvette, France, ²Now at Scripps Institution of Oceanography, UCSD, La Jolla, California, USA, ³Centre National de Recherches Météorologiques, CNRM, Toulouse, France

Abstract Ocean carbon uptake and oxygen content estimates over the past decades suggest that the anthropogenic carbon sink has changed and that the oxygen concentration in the ocean interior has decreased. Although these detected changes appear consistent with those expected from anthropogenic forced climate change, large uncertainties remain in the contribution of natural variability. Using century-long simulations (500–1000 years) of unforced natural variability from six Earth System Models (ESMs), we examine the internally driven natural variability of carbon and oxygen fluxes from interannual to multidecadal time scales. The intensity of natural variability differs between the ESMs, in particular, decadal variability locally accounts for 10–50% of the total variance. Although the variability is higher in all regions with strong climate modes (North Atlantic, North Pacific, etc.), we find that only the Southern Ocean and the tropical Pacific significantly modulate the global fluxes. On (multi)decadal time scales, deep convective events along the Antarctic shelf drive the global fluxes variability by transporting deep carbon-rich/oxygen-depleted waters to the surface and by reducing the sea-ice coverage. On interannual time scales, the global flux is modulated by (1) variations of the upwelling of circumpolar deep waters associated with the southern annular mode in the subpolar Southern Ocean and (2) variations of the equatorial/costal upwelling combined with changes in the solubility-driven fluxes in response to El Niño Southern Oscillation (ENSO) in the tropical Pacific. We discuss the challenges of measuring and detecting long-term trends from a few decade-long records influenced by internal variability.

1. Introduction

Anthropogenically driven changes influence ocean biogeochemistry and marine ecosystems, in particular through the modification of the carbon and oxygen cycles. The ocean uptake of anthropogenic carbon has increased the dissolved inorganic carbon content [Sabine *et al.*, 2004; Khatiwala *et al.*, 2009; Kouketsu and Murata, 2014] leading to seawater acidification [Orr *et al.*, 2005]. In parallel, the oceanic oxygen concentration has decreased as a consequence of global warming, which induces a reduction in solubility and an increase in stratification preventing the supply of oxygen to the ocean interior [Matare *et al.*, 2000; Bopp *et al.*, 2002; Keeling *et al.*, 2010; Helm *et al.*, 2011]. Acidification and deoxygenation may have adverse effects on marine organisms by reducing calcification, triggering physiological stress, and affecting ecosystems distribution and composition [Pörtner, 2008; Bertrand *et al.*, 2010; Prince and Goodey, 2006; Stramma *et al.*, 2011].

In the past decades, numerous studies have focused on quantifying the oceanic content in anthropogenic carbon, leading to the latest estimate of 155 Pg C ± 20% since 1750 [e.g., Khatiwala *et al.*, 2013]. However, large uncertainties remain in the regional rate of ocean carbon uptake, with observations and model studies suggesting either a slow down [e.g., Le Quéré *et al.*, 2007; Schuster *et al.*, 2009] or an increase [Landschützer *et al.*, 2013] of the oceanic uptake of anthropogenic carbon. In addition, recent results indicate that trends in the ocean carbon uptake are likely to be underestimated due to sparse sampling coverage, in particular in the Southern Ocean, which accounts for ∼50% of the total oceanic carbon uptake [Fay and McKinley, 2013; Tjiputra *et al.*, 2014; Majut *et al.*, 2014]. It is therefore still unclear if the detected changes in the rate of carbon uptake can be attributed to climate change or to natural variability [Lovenduski *et al.*, 2008; McKinley *et al.*, 2011; Frölicher *et al.*, 2013; Séférian *et al.*, 2014].

Although the focus on deoxygenation is more recent, the oceanic loss of oxygen over the past decade has been estimated to be ∼40–50 Tmol yr⁻¹ [Keeling *et al.*, 2010; Helm *et al.*, 2011]. Observed changes are

Table 1. CMIP5 Models Used in This Study

Models	piControl Length (Years)	Reference	Acronyms
CESM1-BGC	500	Gent <i>et al.</i> [2011]	CESM
GFDL-ESM2G	500	Dunne <i>et al.</i> [2012]	GFDL-G
GFDL-ESM2M	500	Dunne <i>et al.</i> [2012]	GFDL-M
IPSL-CM5A-LR	1000	Séférian <i>et al.</i> [2012]	IPSL
MPI-ESM-LR	1000	Giorgetta <i>et al.</i> [2013]	MPI-L
MPI-ESM-MR	1000	Giorgetta <i>et al.</i> [2013]	MPI-M

ing at the large decadal variations of oxygen concentrations measured in the North Pacific [Emerson *et al.*, 2004], the Californian Current [Deutsch *et al.*, 2011], and the Humboldt Current [Bertrand *et al.*, 2011]. Quantifying and understanding the natural (internally generated by the climate system itself and externally forced by volcanoes, solar activity, etc.) variability of ocean carbon and oxygen cycles is therefore necessary to put long-term trends into perspective.

Changes in carbon and oxygen content of the global ocean can be approximated by quantifying exchanges of carbon dioxide (CO_2) and oxygen (O_2) at the air-sea interface. This approach does not account for changes in riverine inputs and exchanges at the bottom of the ocean. However, we expect air-sea fluxes to largely drive the variability of the global ocean at interannual and decadal time scales. Numerous studies have estimated air-sea CO_2 fluxes at the global scale using oceanic and atmospheric observations [Takahashi *et al.*, 2002, 2009; Mikaloff Fletcher *et al.*, 2006, 2007; Jacobson *et al.*, 2007; Khatiwala *et al.*, 2009; Gerber *et al.*, 2009; Gerber and Joos, 2010; Rödenbeck *et al.*, 2013; Keeling and Manning, 2014]. In contrast, to our knowledge, only three studies have estimated O_2 air-sea fluxes at the global scale [Najjar and Keeling, 2000; Garcia and Keeling, 2001; Gruber *et al.*, 2001]. However, these studies are limited by the length of the observational record and only resolve part if any of the internal variability from interannual to decadal time scales.

In a recent study, Séférian *et al.* [2013] used a long-term (1000 year) experiment with the IPSL-CM5A-LR Earth System Model (ESM) to evaluate the internal variability of air-sea CO_2 fluxes. They found large variability on multidecadal time scales driven by changes in sea surface temperatures (SST) in the North Atlantic and by changes in the vertical supply of dissolved inorganic carbon in the North Pacific and the Southern Ocean. In this study, we extend this analysis by considering six different ESMs and examining jointly the variability of CO_2 and O_2 air-sea fluxes. Using preindustrial experiments excluding changes in anthropogenic and natural radiative forcing variability, we quantify the internal variability of CO_2 and O_2 air-sea fluxes and examine which regions and processes are controlling this variability.

2. Methods

We use the latest generation of projections performed by six ESMs in the frame of the Coupled Model Intercomparison Project 5 (CMIP5) [Taylor *et al.*, 2012]. All ESMs include the major components of the climate system (ocean, atmosphere, and land-surface) and a marine biogeochemical module simulating the carbon and oxygen cycles (see Table 1). Here we focus on the six ESMs with a preindustrial experiment called piControl lasting at least 500 years, which allows for statistically robust results from interannual to multidecadal time scales. To facilitate intermodel comparison, all variables were interpolated onto a common $1^\circ \times 1^\circ$ regular grid using a Gaussian weighted average and to standard ocean depths (World Ocean Atlas levels) using linear interpolation. Drift due to model adjustment was removed using a temporal linear regression for each variable. For clarity, we use simplified acronyms to identify the six ESMs (Table 1).

Internal variability was examined using statistical tools and spectral analysis, including standard deviation to quantify interannual variability, decadal-to-interannual ratios to examine the proportion of variability occurring on decadal time scales, and power spectrum variance to highlight the frequencies of highest variability. The spatial patterns in regions of highest variability were described using empirical orthogonal functions (EOFs) and principal component analysis (PCA) of both CO_2 and O_2 fluxes. The correlation between the leading EOFs principal components (PCs) and other physical and biogeochemical variables such as MLD, SST, wind stress, and net primary production (PP) was used as an indicator of potential processes

consistent with what is expected from climate change in most regions of the ocean [Andrews *et al.*, 2013]. However, the uncertainties of the estimated trends are still large (at least $\pm 25\%$). The major limitation comes from the insufficient spatiotemporal coverage of observations to disentangle the anthropogenically driven trend from the natural variability at interannual and decadal time scales [Keller *et al.*, 2014]. The challenge of estimating long-term trends from records of a few decades is striking when looking at the large decadal variations of oxygen concentrations measured in the North Pacific [Emerson *et al.*, 2004], the Californian Current [Deutsch *et al.*, 2011], and the Humboldt Current [Bertrand *et al.*, 2011]. Quantifying and understanding the natural (internally generated by the climate system itself and externally forced by volcanoes, solar activity, etc.) variability of ocean carbon and oxygen cycles is therefore necessary to put long-term trends into perspective.

Changes in carbon and oxygen content of the global ocean can be approximated by quantifying exchanges of carbon dioxide (CO_2) and oxygen (O_2) at the air-sea interface. This approach does not account for changes in riverine inputs and exchanges at the bottom of the ocean. However, we expect air-sea fluxes to largely drive the variability of the global ocean at interannual and decadal time scales. Numerous studies have estimated air-sea CO_2 fluxes at the global scale using oceanic and atmospheric observations [Takahashi *et al.*, 2002, 2009; Mikaloff Fletcher *et al.*, 2006, 2007; Jacobson *et al.*, 2007; Khatiwala *et al.*, 2009; Gerber *et al.*, 2009; Gerber and Joos, 2010; Rödenbeck *et al.*, 2013; Keeling and Manning, 2014]. In contrast, to our knowledge, only three studies have estimated O_2 air-sea fluxes at the global scale [Najjar and Keeling, 2000; Garcia and Keeling, 2001; Gruber *et al.*, 2001]. However, these studies are limited by the length of the observational record and only resolve part if any of the internal variability from interannual to decadal time scales.

In a recent study, Séférian *et al.* [2013] used a long-term (1000 year) experiment with the IPSL-CM5A-LR Earth System Model (ESM) to evaluate the internal variability of air-sea CO_2 fluxes. They found large variability on multidecadal time scales driven by changes in sea surface temperatures (SST) in the North Atlantic and by changes in the vertical supply of dissolved inorganic carbon in the North Pacific and the Southern Ocean. In this study, we extend this analysis by considering six different ESMs and examining jointly the variability of CO_2 and O_2 air-sea fluxes. Using preindustrial experiments excluding changes in anthropogenic and natural radiative forcing variability, we quantify the internal variability of CO_2 and O_2 air-sea fluxes and examine which regions and processes are controlling this variability.

explaining these patterns. The regional variability was also examined in relation to the main climate modes: the Southern Annular Mode (SAM) in the Southern Ocean and El Niño-Southern Oscillation (ENSO) in the tropical Pacific. SAM is represented by the Southern Annular Mode index (SAMi) (difference between the normalized monthly zonal mean sea level pressure between 40°S and 70°S [Nan and Li, 2003]) and ENSO by the Nino3.4 index (as defined by NOAA at <http://www.esrl.noaa.gov/psd/data/climateindices/list/>). Note that those indexes were computed using annual means instead of monthly means. The amplitude of the variability is damped compared to a monthly index, but it has been performed for both model results and observations and therefore does not affect the intercomparison. Details on the statistical tools, spectral analysis, and EOFs can be found in Appendix A.

3. Results

3.1. Spatial Patterns of CO₂ and O₂ Air-Sea Fluxes and Evaluation Against Available Estimates

Maps of the six CMIP5 models internal CO₂ and O₂ annual air-sea fluxes (e.g., FCO₂ and FO₂) are shown in Figure 1. We evaluate these fluxes against the available estimates at the global scale, which were obtained by the assimilation of oceanic observations with inverse methods [Gruber *et al.*, 2001; Mikaloff Fletcher *et al.*, 2007; Gerber and Joos, 2010]. Mikaloff Fletcher *et al.* [2007] and Gerber and Joos [2010] combined total carbon data and an estimate of anthropogenic carbon to compute the preindustrial contribution to the total CO₂ air-sea flux. Gruber *et al.* [2001] estimated the total O₂ flux, which does not separate the internal from the anthropogenic contribution. Changes in O₂ atmospheric concentrations due to anthropogenic activities (fossil fuel burning and land use) are estimated to be less than 0.1% [Keeling and Manning, 2014]. Changes in O₂ oceanic concentrations due to climate change are of the order of $\sim 40 \text{ Tmol yr}^{-1}$, based on a O₂-to-heat ratio of 5–7 nmol O₂ J⁻¹ and a warming of $6 \times 10^{21} \text{ J yr}^{-1}$ [Plattner *et al.*, 2002; Bopp *et al.*, 2002; Matear and Hirst, 2003; Keeling *et al.*, 2010], which represents less than 1‰ of the O₂ content in surface waters (<100 m). We therefore assume that the total O₂ flux is a good approximation of the natural component. CMIP5 climate models reproduce similar patterns as those derived by Mikaloff Fletcher *et al.* [2007] and Gruber *et al.* [2001] (Figure 2). Note that the fluxes of Gerber and Joos [2010] are not shown in Figure 2 as they agree within the uncertainties with those of Mikaloff Fletcher *et al.* [2007]. Both CO₂ and O₂ are outgassing (negative fluxes) in tropical and equatorial regions and ingassing (positive fluxes) in the North Atlantic and Arctic Oceans, where solubility effects dominate the air-sea exchanges. Indeed, CO₂ and O₂ solubility increases with decreasing temperature (Figures 1 and 2). In the Southern Ocean, CO₂ flux and O₂ flux anticorrelation highlights the signature of circumpolar deep waters upwelling and deep mixing both transporting deep carbon-rich and O₂-depleted waters to the surface, leading to CO₂ outgassing and O₂ ingassing. These physical processes are further modulated by primary production that consumes dissolved inorganic carbon (DIC) and produces O₂ favoring CO₂ ingassing and O₂ outgassing, which is identifiable in the South Atlantic for example (Figures 1 and 2).

Most differences between CMIP5 and inversion fluxes are related to differences in the spatial distribution of the fluxes, which cancel out when averaged over several regions. For example, the O₂ oceanic uptake in the Atlantic Ocean is dominated by the temperate North Atlantic in Gruber *et al.* [2001] and by the North Atlantic in the CMIP5 models (Figure 2). In that case, the difference arises from the position of the spring phytoplankton bloom and of winter convection sites, which mostly occur north of the limit between the two regions (58°N) in CMIP5 models. Largest uncertainties in both data-based and model estimates are located in the Southern Ocean (Figure 2). This is due to the lack of observations in this region and the difficulties met by climate models to reproduce the complex physical processes related to the formation of ice and Antarctic bottom waters along the Antarctic shelf, the upwelling of circumpolar deep waters, and the subduction of mode and intermediate waters [Sallée *et al.*, 2013a].

3.2. Regional Variability From Interannual to Decadal Time Scales

These annual air-sea fluxes are modulated by internal variability from interannual to decadal time scales. When considering each ESM individually, the patterns of interannual variability are very similar for both FCO₂ and FO₂ (Figure 3). Highest interannual variability in CO₂ and O₂ fluxes is found in the North Pacific Ocean, the North Atlantic Ocean, and the Southern Ocean, where it reaches 5–15 g C m⁻² yr⁻¹ for FCO₂ and 2–6 mol O₂ m⁻² yr⁻¹ for FO₂ (Figure 3). The equatorial Pacific also stands out as a region of interannual variability, in particular in three of the ESMs: CESM, GFDL-G, and GFDL-M, where it reaches 5–10 g C m⁻²

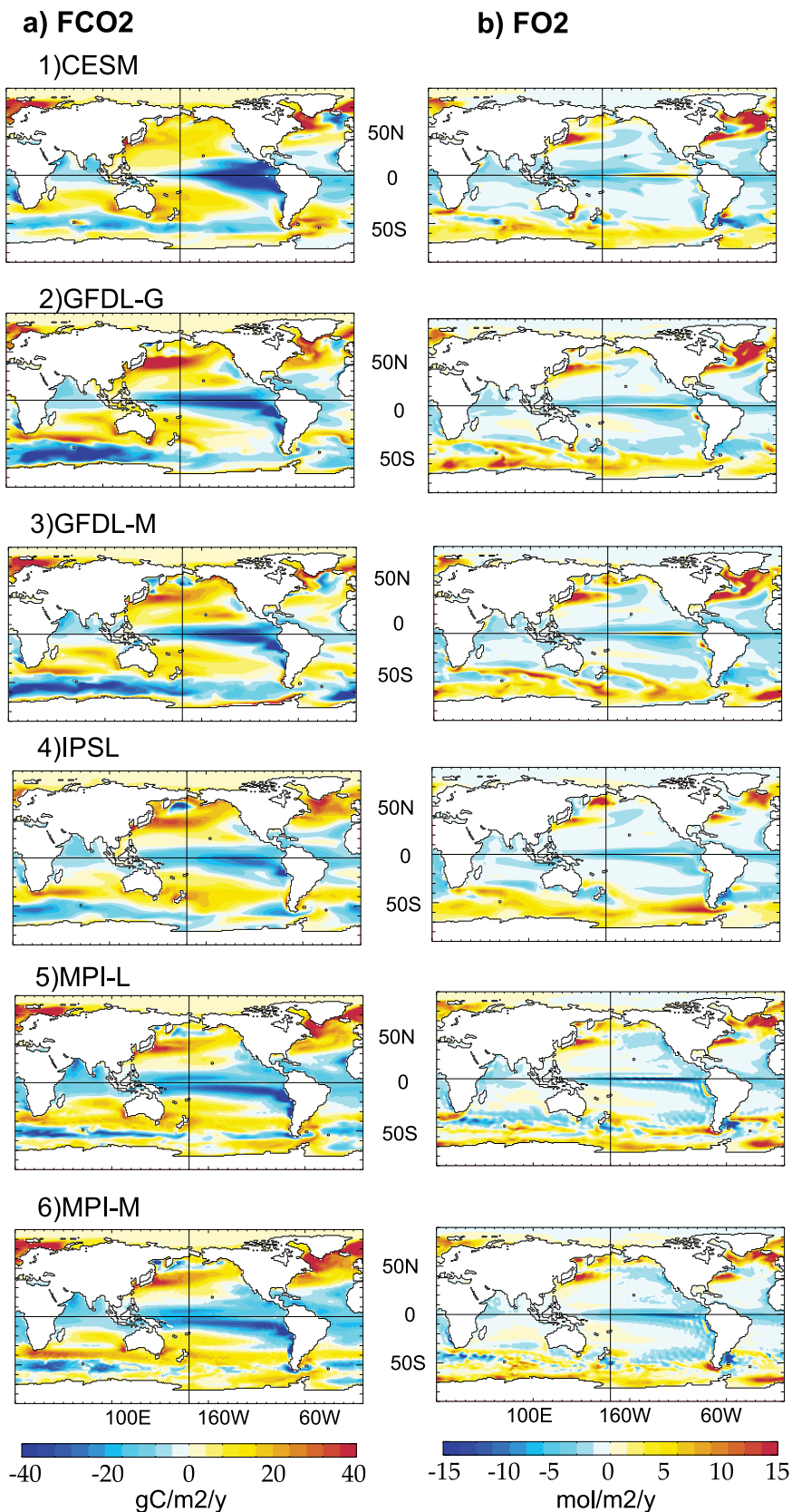


Figure 1. Maps of annual mean air-sea (a) CO₂ flux (in gC m⁻² yr⁻¹) and (b) O₂ flux (in mol O₂ m⁻² yr⁻¹) in the piControl simulations. Positive fluxes are toward the ocean.

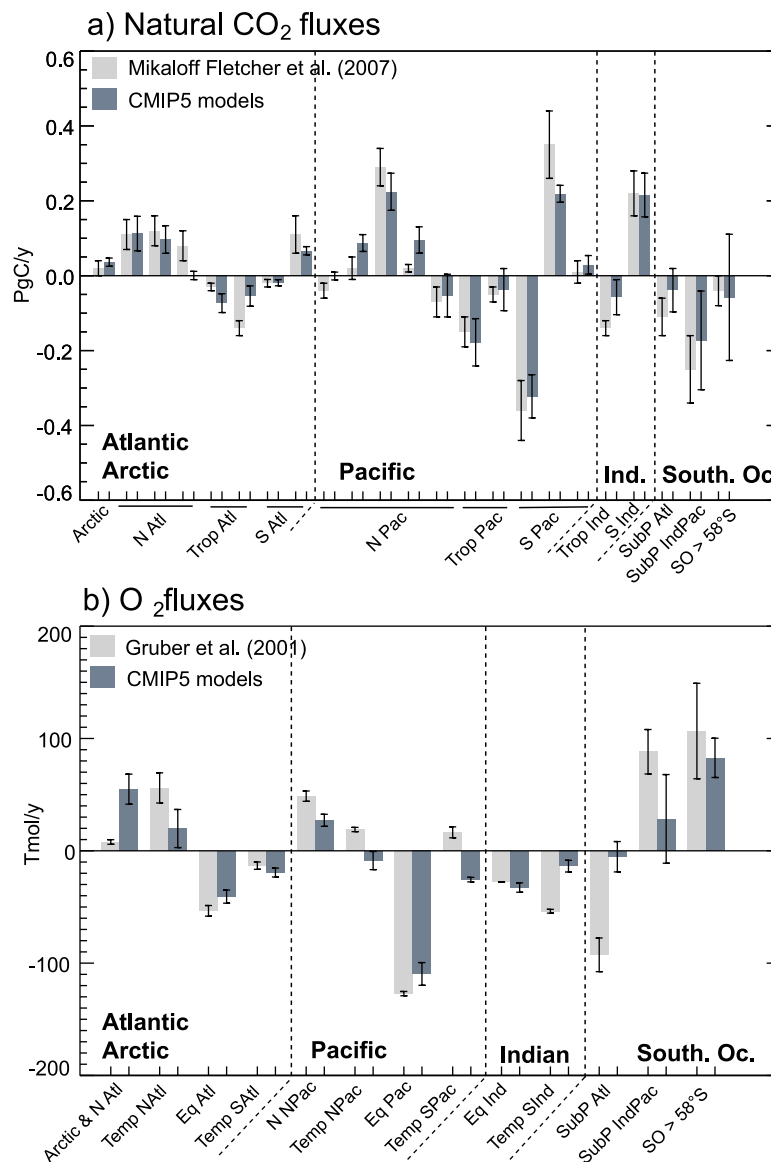


Figure 2. Mean global CO₂ and O₂ fluxes for the six CMIP5 models compared to inversion-based estimates from Mikaloff Fletcher et al. [2007] and Gruber et al. [2001]. Error bars indicate the standard deviation between models for CMIP5 fluxes or between the various estimates obtained from inverse methods (spread between circulation models in Mikaloff Fletcher et al. [2007] and constrained versus unconstrained balance in Gruber et al. [2001]). Regions are those defined in Mikaloff Fletcher et al. [2007] and Gruber et al. [2001], respectively.

yr⁻¹ for FCO₂ and 2–4 mol O₂ m⁻² yr⁻¹ for FO₂. Although the variability is similar at the basin scale between the six ESMs, each one presents specific spatial structures corresponding to its ocean circulation patterns. For example, we will show in section 3.4 that patches of intense variability south of 60°S correspond to deep convection sites.

The proportion of this variability occurring on decadal to multidecadal time scales is identified using the decadal-to-interannual ratio called diagnosed potential predictability (DDP) [Boer, 2004], described in Appendix A. The DDP shown in Figure 4 maps the contribution of the variability on temporal scales of 20 years compared to the total interannual variability. One striking result is the tremendous spread observed in the decadal-to-interannual ratios between the different models (Figure 4). While the variability on 20 year time scales is relatively low everywhere in CESM, MPI-L, and MPI-M (DDP < 10%), it represents locally 20–30% and up to 50% of the interannual variance in the North Atlantic and the Southern Ocean in the GFDL-G, GFDL-M, and IPSL models.

Interannual standard deviation

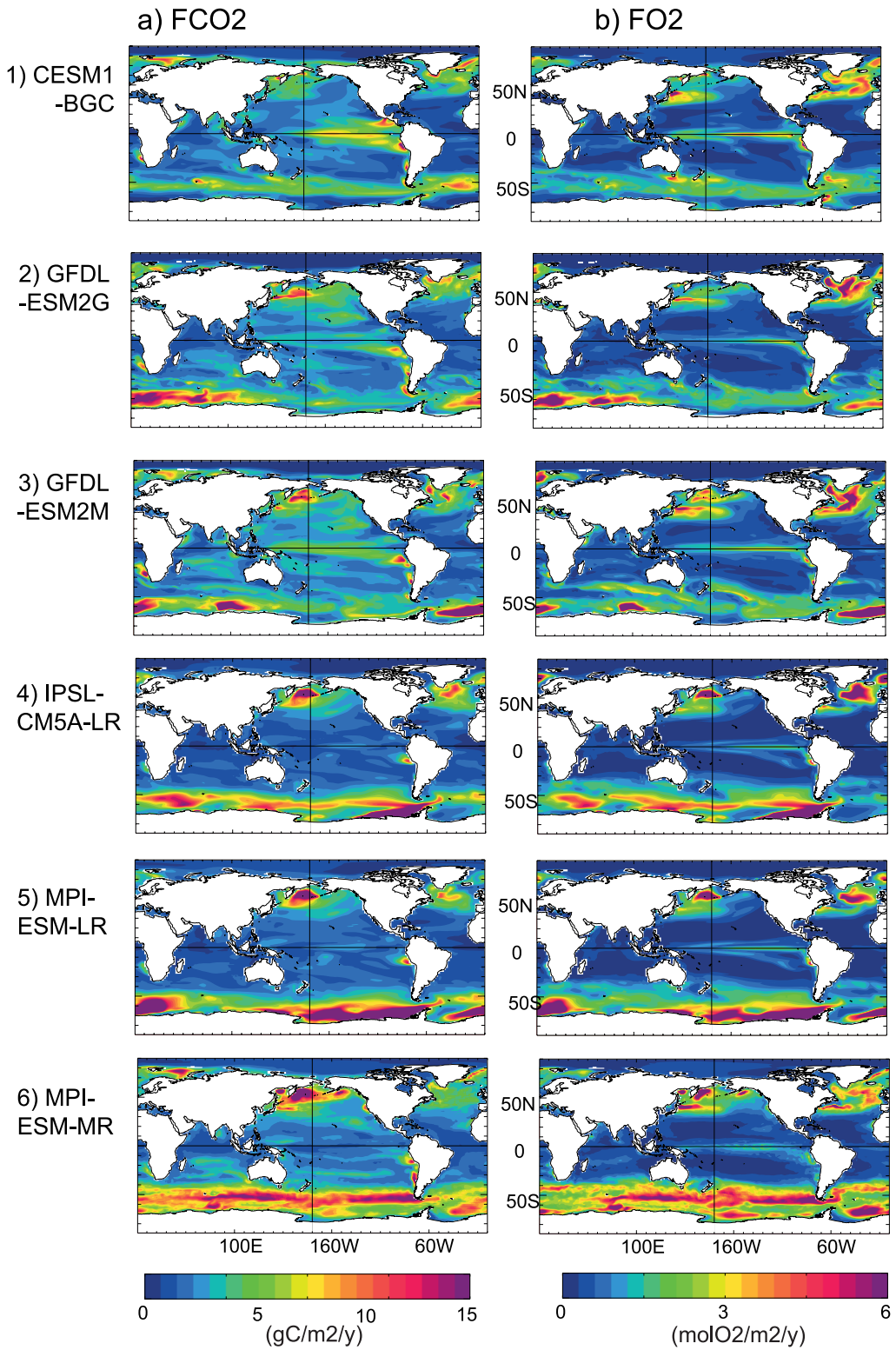


Figure 3. Standard deviation at interannual time scales for (a) FCO₂ and (b) FO₂ in the six ESMs.

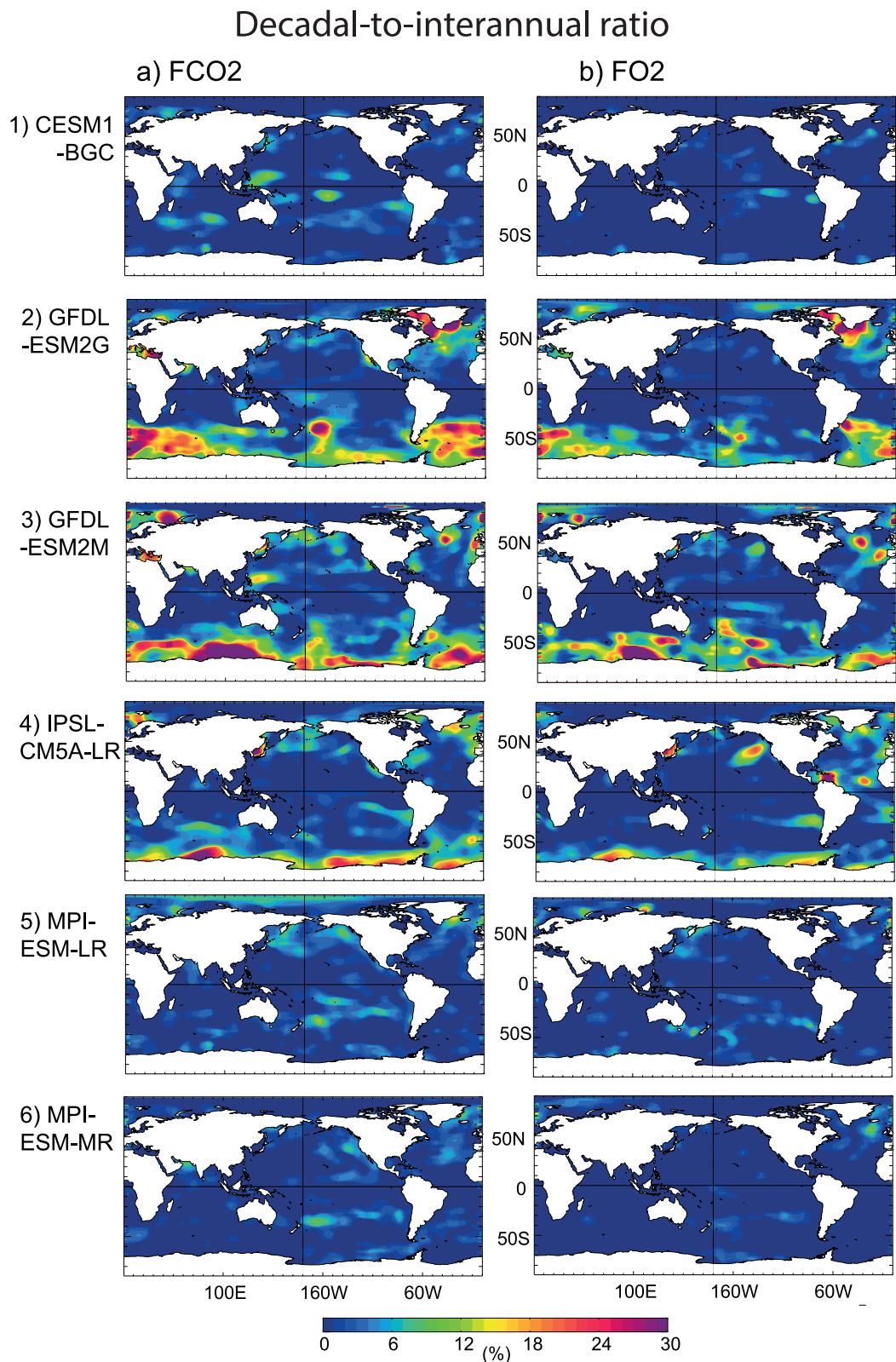


Figure 4. Decadal-to-interannual variance ratio or DDP (in %) for (a) FCO₂ and (b) FO₂ in the six ESMs. The DDP highlights regions and models of high decadal variability with a period of 20 years. See equation (A1) in Appendix A.

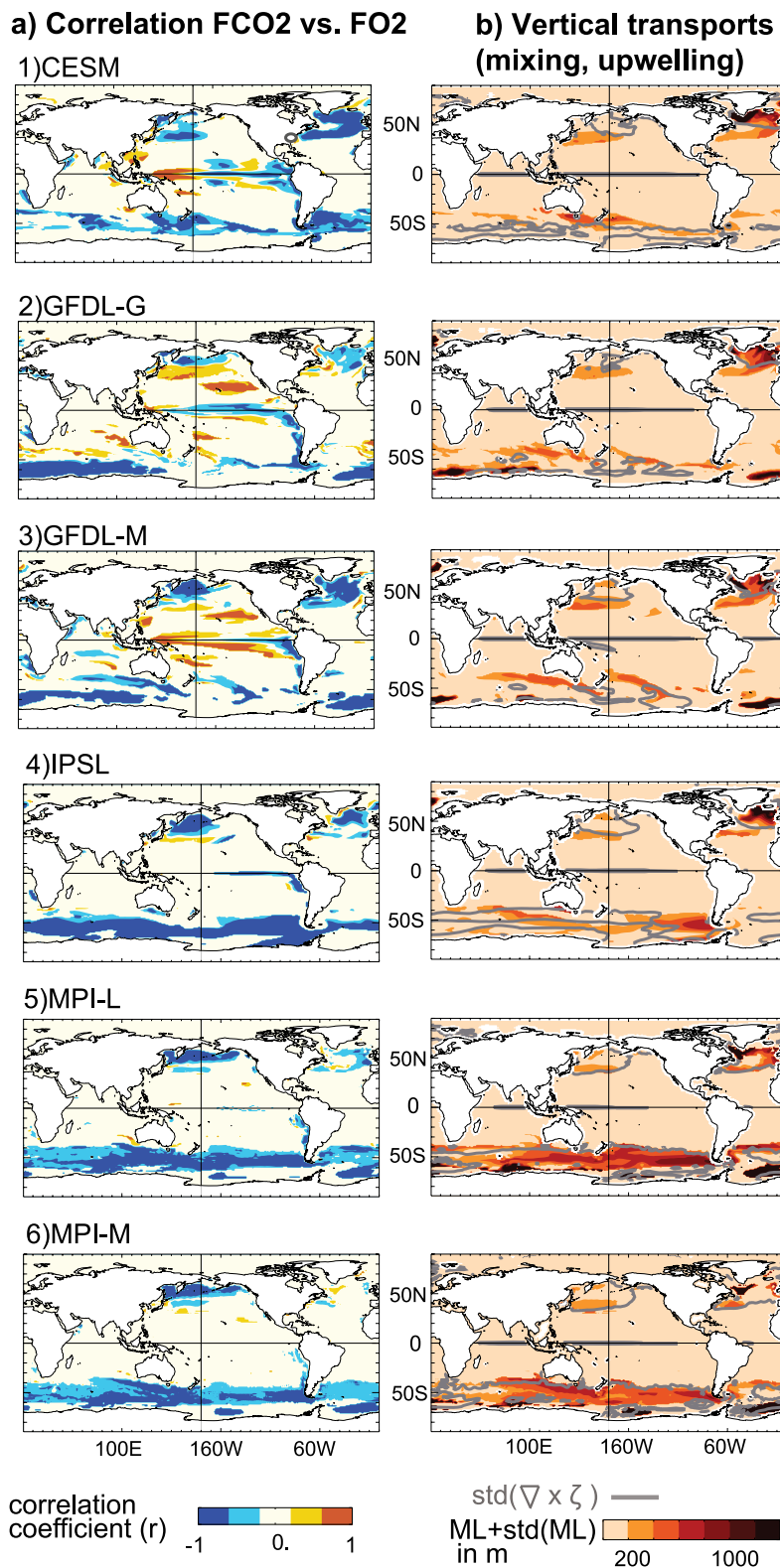


Figure 5. (a) Correlation between FCO₂ and FO₂ in regions of highest variability (80th percentile of the standard deviation); (b) variability of the vertical transport. Changes in mixing are indicated by the variability of the mixed layer (ML), where the ML is relatively deep (ML+std(ML), color shading). Changes in upwelling are indicated with the variability of the wind curl in areas where it is positive (std($\nabla \times \zeta$), gray contours). See Appendix A.

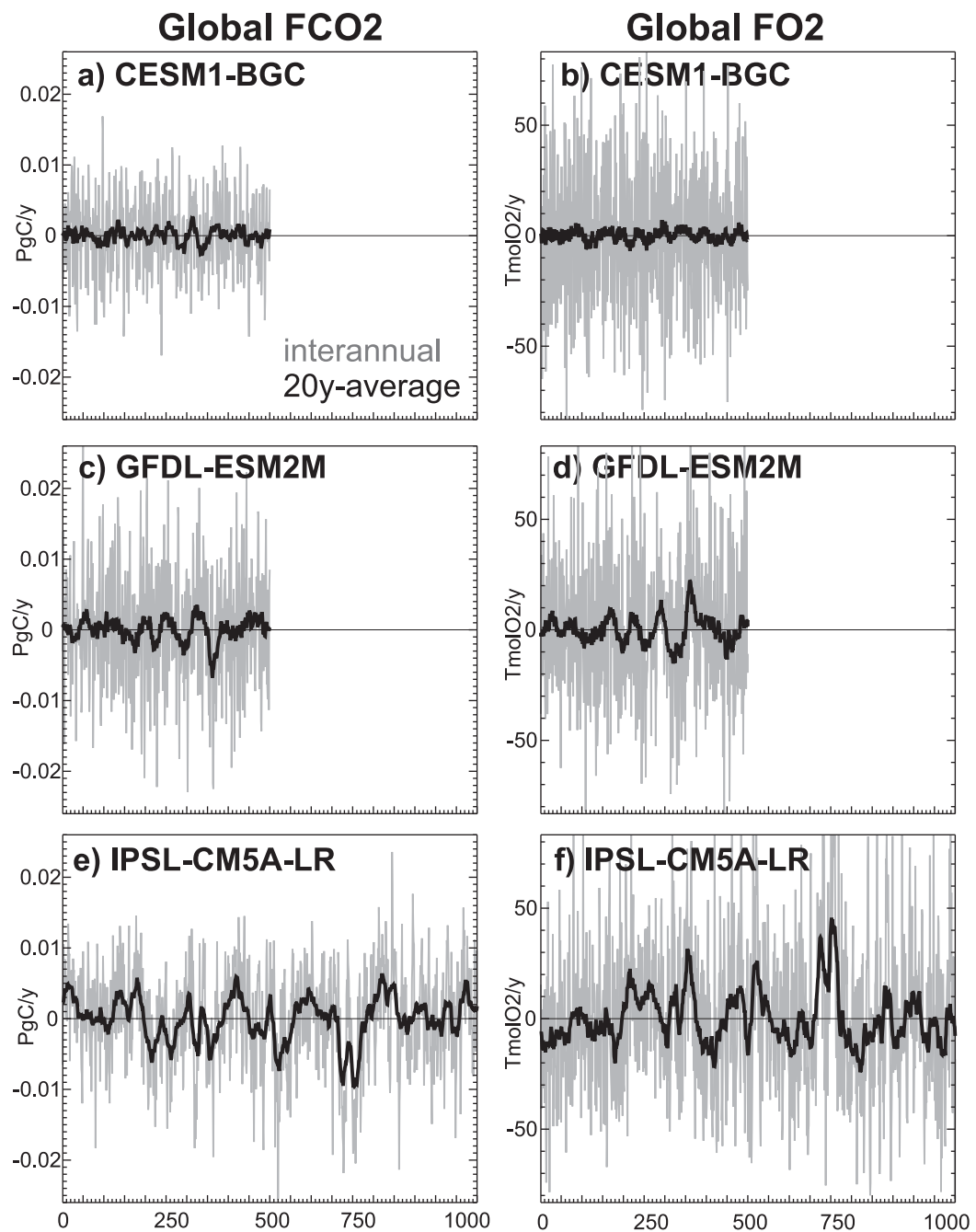


Figure 6. Time series of air-sea CO₂ flux (in Pg C yr⁻¹) and O₂ flux (in mol Tmol O₂ yr⁻¹) for three models (CESM, GFDL-M, and IPSL) on interannual time scales (gray) and on decadal time scales (black, 20 year sliding average).

The coupling between FCO₂ and FO₂ in regions of highest variability provide useful insights on which processes dominate the variability (Figure 5a). A strong negative correlation between FCO₂ and FO₂ indicates that either vertical transport or biological activity is dominating the variability of air-sea fluxes. Vertical transport of deep DIC-rich and O₂-depleted waters to the surface leads to CO₂ outgassing and O₂ ingassing, while enhanced primary production consumes DIC and releases O₂, leading to CO₂ ingassing and O₂ outgassing. Changes in vertical transport associated with mixing and upwelling are, respectively, identified using the variability of the mixed layer depth and the variability of the wind curl in areas where it is positive (Figure 5b).

Most patterns of strong internal variability and strong anticorrelation between FCO₂ and FO₂ ($r < -0.6$) coincide with regions of variable vertical transport. High variability patches of FCO₂ and FO₂ are associated

Variability $V(f)$

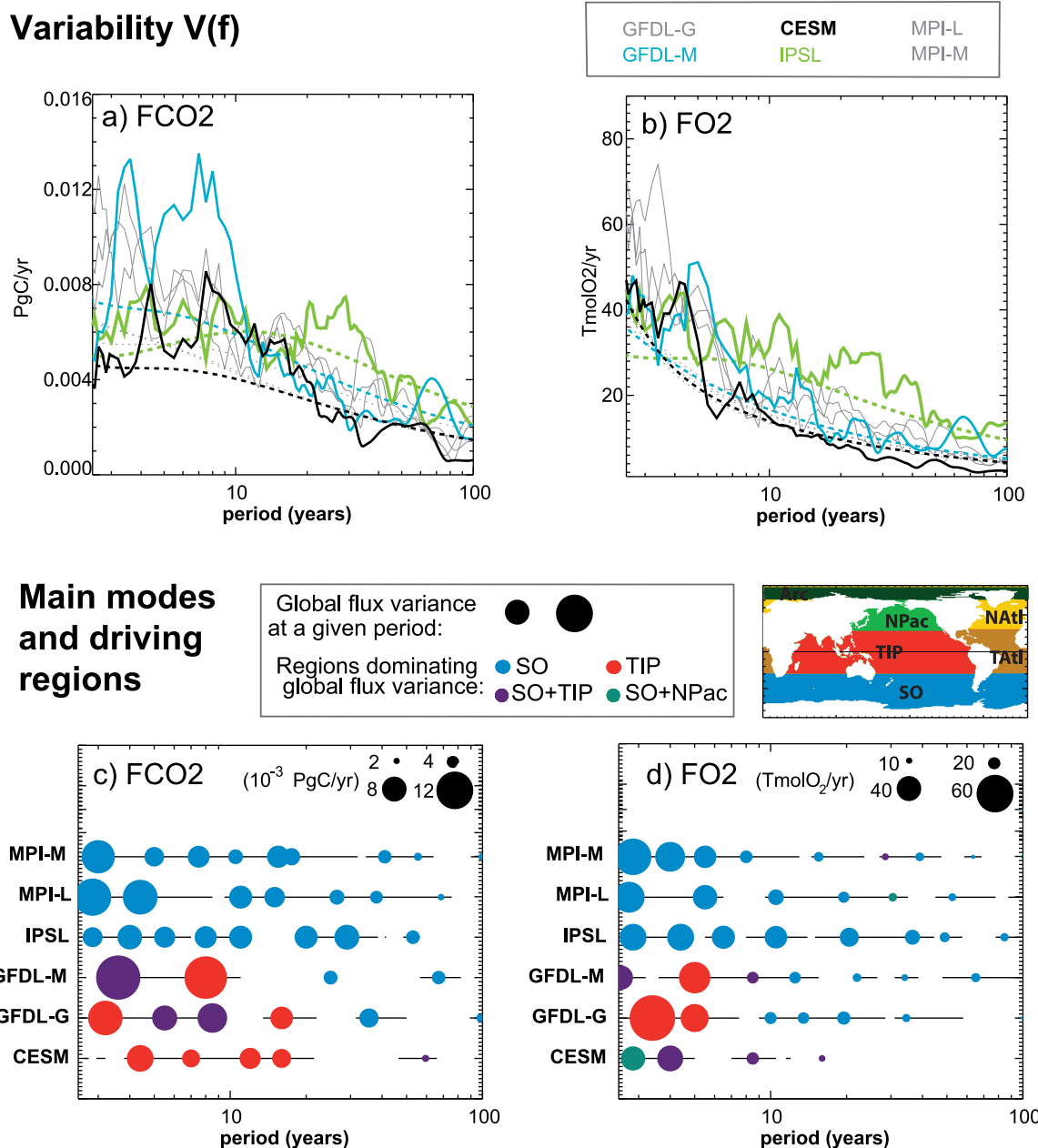


Figure 7. Variability $V(f)$ of (a) CO₂ and (b) O₂ global air-sea fluxes at each frequency for the six CMIP5 models. Three models are highlighted and discussed in the text. Main modes and driving regions of internal variability for (c) CO₂ and (d) O₂ global air-sea fluxes. Amplitudes and periods are quantified with $V(f)$ (symbols size). For each peak, colors indicate the dominant regions contributing to the variability (codominance occurs if the contribution of two regions differ by less than 10%). SO: Southern Ocean, TIP: Tropical Indo-Pacific, NPac: North Pacific. Limits between the regions are shown on the inserted map. Black lines indicate when the spectrum is significant, i.e., the amplitude is greater than the amplitude of the AR1 spectrum. Details of the method can be found in section A3.

with variations in deep convection sites in the North Atlantic and along the Antarctic shelf ($ML + std(ML) > 1000$ m), mode and intermediate water formation sites at midlatitude and high latitude ($ML + std(ML) > 200$ m) and around upwelling areas in the equatorial Pacific and the subantarctic region (gray contours, Figure 5b). Variability in ocean circulation and vertical transport thus strongly modulates FCO₂ and FO₂ internal variability from interannual to decadal time scales. Note that the region of high variability in the tropical Pacific extends further than the upwelling region and covers all areas under the influence of the El Niño Southern Oscillation (ENSO). This is explained by the strong contribution of horizontal advection in that region, which transports anomalies away from the upwelling. Although it is difficult to diagnose, biological activity is likely modulating FCO₂ and FO₂ in areas where the anticorrelation is weak

Table 2. Regions, Processes, and Periods Driving Global Air-Sea Fluxes Internal Variability^a

Models	Tropical Pacific	Southern Ocean		
		Subpolar	Polar	
CESM	ENSO (Upw./Solub.)	SAM (Upw./Bio.)		
	4–10 year	3–4 year; 10 year		
GFDL-G	ENSO (Upw./Solub.)	SAM (Upw./Bio.)	Deep convection	
	4–10 year	6–10 year; 30 year	30–40 year	
GFDL-M	ENSO (Upw./Solub.)	SAM (Upw.)	Deep convection	
	4–10 year	3–4 year; 20 year	20 year; 60 year	
IPSL		SAM (Upw.)	Deep convection	
		4 year; 10 year	20 year; 50–60 year	
MPI-L		SAM (Upw./Bio.)	Deep convection	
		3–4 year	30–40 year	
MPI-M		SAM (Upw./Bio.)	Deep convection	
		3–4 year	20–30 year	

^aProcesses are inferred from the EOF analysis presented in Figures 8–10 and in supporting information Figures fs03–fs10. Processes are deep convection events and mechanisms associated with ENSO and SAM climate modes: upwelling (Upw.), solubility (Solub.), and biological production (Bio.). Periods of highest variability are determined by computing the spectral variance $V(f)$ for each EOF (see section A4).

($-0.6 < r < 0$), such as in the midlatitudes, in the tropical Pacific and the subantarctic region (Figure 5b). The contribution of biology will be further discussed in section 3.4.

Finally, a strong positive correlation between FCO_2 and FO_2 indicates that solubility dominates the variability in the air-sea exchanges leading to the outgassing or ingassing of both CO_2 and O_2 . Solubility drives strong internal variability in the tropical Pacific and north Pacific in CESM, GFDL-G, and GFDL-M (Figures 5a1–5a3). In three other models, IPSL, MPI-L, and MPI-M, the variability in the tropical and north Pacific and hence the contribution of solubility to internal variability is relatively low (Figure 3).

3.3. How Does Regional Variability Impact Global Fluxes?

The differences in the relative contribution of decadal variability compared to interannual variability at the regional scale largely impact the internal variability of the global air-sea fluxes. Figure 6 presents the time series of the interannual and decadal (20 year sliding average) global CO_2 and O_2 air-sea fluxes as simulated by three ESMs that present very contrasted variability at interannual and decadal time scales (CESM, GFDL-M, and IPSL; Figures 3 and 4). The amplitude of global interannual variability is relatively similar between the three models (gray lines in Figure 6). However, the striking difference is the amplitude of the decadal variability that clearly increases from CESM to GFDL-M and finally to IPSL (black line in Figure 6). In order to examine the global air-sea fluxes from interannual to multidecadal time scales in the six ESMs more quantitatively, we use spectral analysis to detect the major modes of variability and to quantify their periodicity and amplitude. This broadens the results highlighted by the time series to all temporal scales from interannual to multidecadal.

The amplitude of the variability $V(f)$ of global FCO_2 and FO_2 expected at each frequency is computed by integrating the power spectral density (PSD) over small-frequency intervals (see section A3). The analysis of $V(f)$ confirms that the temporal scales and the amplitude of internal variability vary amongst the ESMs (Figures 7a and 7b). When focusing on the three ESMs mentioned previously: IPSL exhibits intense decadal and multidecadal variability on time scales between 10 and 80 years, with amplitudes up to 4 Tg C yr^{-1} for FCO_2 and $10\text{--}20 \text{ Tmol O}_2 \text{ yr}^{-1}$ for FO_2 . In contrast, GFDL-M shows substantial variability at shorter time scales between 2 and 20 years, leading to tremendous interannual variations of about $6 \times 10 \text{ Tg C yr}^{-1}$ for FCO_2 and $25 \text{ Tmol O}_2 \text{ yr}^{-1}$ for FO_2 . Finally, CESM exhibits a much lower internal variability on decadal time scales, in particular FO_2 that shows significant variability only on time scales shorter than 10 years (Figures 7a and 7b).

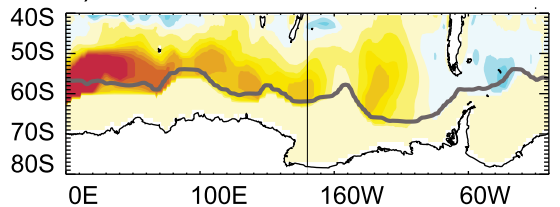
To emphasize on the major modes of variability and compare the six ESMs, we only retain the significant peaks of $V(f)$, i.e., with an amplitude larger than the first-order autoregressive process. For example, the two large peaks of GFDL-M present for the variability of FCO_2 at periods of 3–4 and 7–9 years are retained as the major modes of variability on interannual time scales in this model (symbol size in Figure 7c).

FCO_2 and FO_2 highest variability modes are found at interannual time scales, with maximum amplitudes of $\sim 6\text{--}12 \text{ Tg C yr}^{-1}$ for FCO_2 and $\sim 40\text{--}60 \text{ Tmol O}_2 \text{ yr}^{-1}$ for FO_2 (Figures 7c and 7d). On decadal and multidecadal time scales, FCO_2 and FO_2 generally display 2–4 significant modes of variability reaching $\sim 4\text{--}6 \text{ Tg C yr}^{-1}$ and $\sim 10\text{--}30 \text{ Tmol O}_2 \text{ yr}^{-1}$, respectively. Note that the variability of FCO_2 and FO_2 at the global scale is not perfectly in phase (Figures 7c and 7d). Indeed, the global flux integrates a wide range of processes that are coupled at the local scale but compensate each other when considering the variations at the global scale.

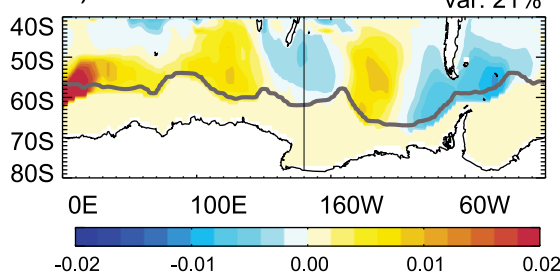
Although the ESMs share similar behaviors with highest variability occurring at 3–8 year periods and decreasing toward longer time scales, each ESM develops its own mode of variability characterized by

GFDL-M Sub-polar region

a) FCO₂-EOF1 var: 23%



b) FO₂-EOF1 var: 21%



c) Correlations PC

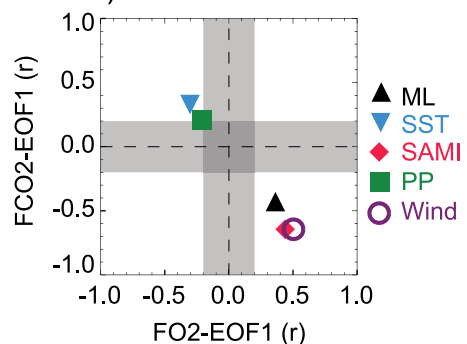
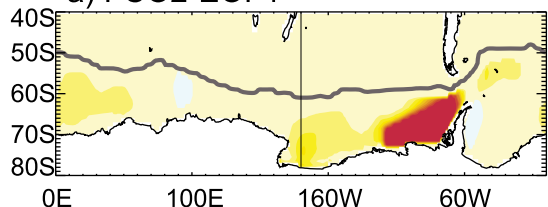


Figure 8. Spatial patterns of the first EOF of (a) FCO₂ and (b) FO₂ in the GFDL-M model in the subpolar Southern Ocean. The subpolar domain is delimited by the 10% annual ice coverage (gray line). (c) Relationship between the principal component PC1 of FCO₂ and FO₂ and other variables (MLD, SST, PP, wind stress, and SAMI climate index) are identified using the linear correlation coefficients (*r*). Gray shading masks low correlations.

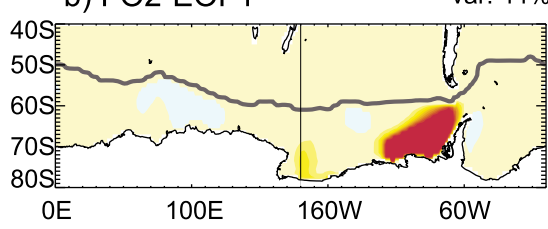
different periods and amplitude. Part of the differences in amplitude and period are likely explained by the differences in the regions driving the variability. The oceanic regions contributing the most to each mode of variability were identified (colors in Figure 7, see section A3 for details). Although the variability is strong in the North Pacific and North Atlantic basins, the Southern Ocean and Tropical Indo-Pacific dominate the internal variability of the global fluxes. Indeed, those two regions combine strong local variability (Figures 4c–4f) with areas much larger than those of the northern basins. On decadal time scales, we find that the

IPSL Polar region

a) FCO₂-EOF1 var: 43%



b) FO₂-EOF1 var: 44%



c) Correlations PC

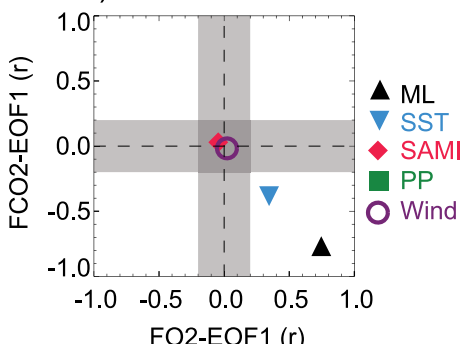


Figure 9. Spatial patterns of the first EOF of (a) FCO₂ and (b) FO₂ in the IPSL model in the polar Southern Ocean. The polar domain is delimited by the 10% annual ice coverage (gray line). (c) Relationship between the principal component PC1 of FCO₂ and FO₂ and other variables (MLD, SST, PP, wind stress, and SAMI climate index) are identified using the linear correlation coefficients (*r*). Gray shading masks low correlations.

CESM1-BGC

Tropical Pacific

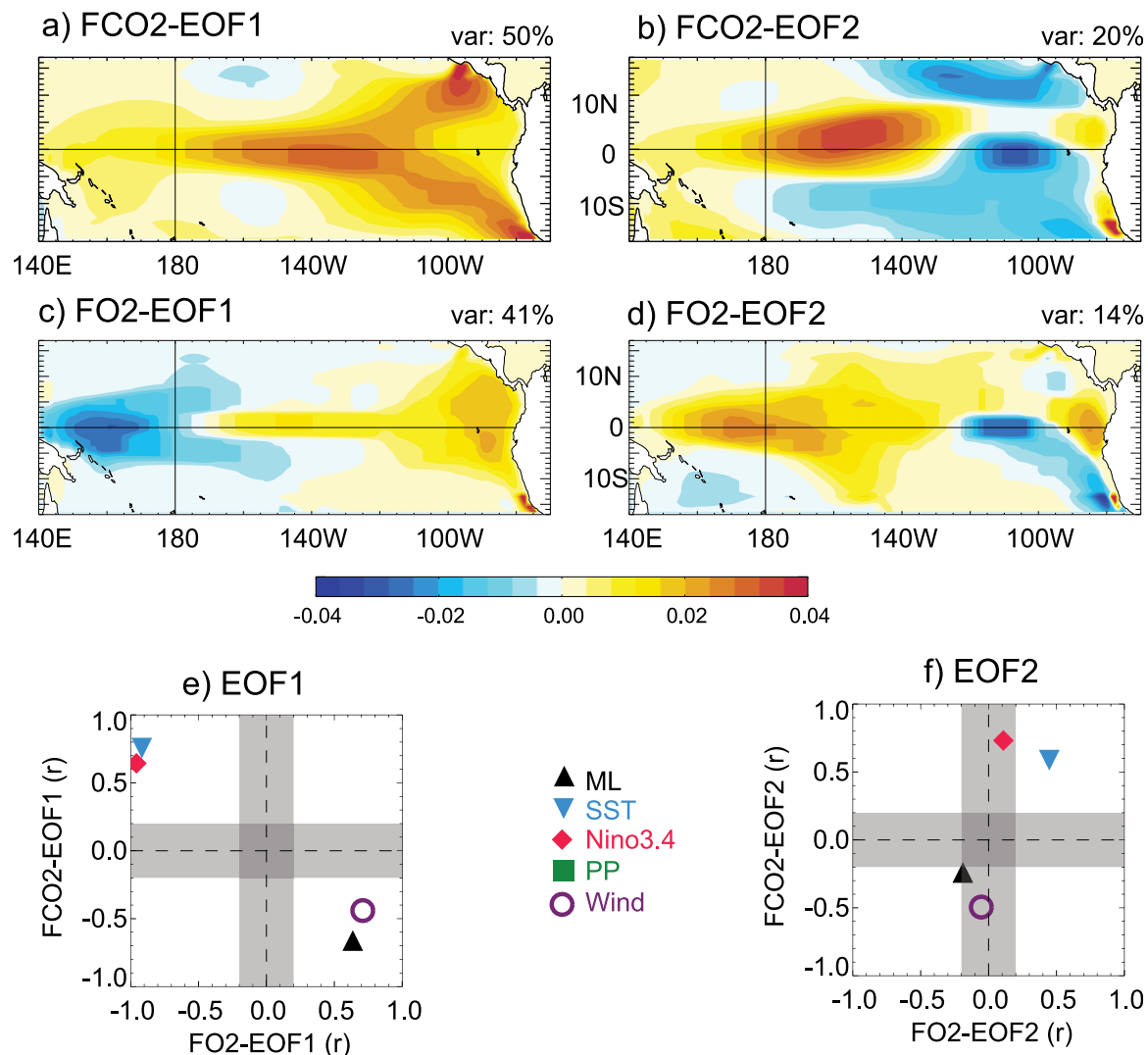


Figure 10. First two leading EOFs in the CESM model in the Tropical Pacific. Spatial patterns of EOF1 and EOF2 for (a and b) CO₂ fluxes and (c and d) O₂ fluxes. (e and f) Relationship between the principal component PC1 of FCO₂ and FO₂ and other variables (MLD, SST, PP, wind stress, and Niño3.4 climate index) are identified using the linear correlation coefficients (r). Gray shading masks low correlations.

internal variability is largely driven by the Southern Ocean, whereas on interannual time scales, it is controlled either by the Southern Ocean, the Tropical Indo-Pacific, or a combination of both regions (Figure 7).

CESM, GFDL-G, and GFDL-M are characterized by very energetic modes of variability on interannual time scales associated with a strong contribution of the Tropical Indo-Pacific region (Figure 7). However, GFDL models display some variability associated with the Southern Ocean on decadal time scales, whereas CESM stands out by its very low variability for periods longer than 18 years, confirming the results obtained with the DDP (Figures 4a and 4b). In contrast, IPSL, MPI-L, and MPI-M are largely dominated by the variability in the Southern Ocean across all time scales. MPI models are, however, dominated by very energetic modes on interannual time scales, whereas the IPSL model shows a series of modes of similar variance from interannual to multidecadal time scales. Note that both MPI ESMs display variability on decadal time scales even though their DDP at a 20 year period was very low. The wide spread in the period and amplitude between the ESMs highlights the strength of the spectral analysis compared to a simpler approach focusing only on one period such as the DDP.

3.4. Key Role of the Southern Ocean and Tropical Pacific

In the following, we focus on the mechanisms explaining air-sea fluxes variability in the two regions driving the variability at the global scale. The processes in the Southern Ocean and tropical Pacific are examined using EOFs and the relation between the associated principal components (PCs), climate modes, and other physical and biogeochemical variables (MLD, SST, wind stress, and PP). For clarity, we first discuss three models that exhibit the stronger regional responses, i.e., in which the variance explained by the first mode is the highest (see supporting information Figure fs02). EOFs of all the models are provided in supporting information (Figures fs03–fs10) and are used to generalize the results in Table 2. The current analysis focuses on the first PC in the Southern Ocean and on the first two PCs in the tropical Pacific, the variance explained by the following EOFs rapidly dropping below 5% (see section A4 for details on the method). The Southern Ocean contributes to the variability at the global scale via two major processes: (1) the response to the SAM in the subpolar region and (2) deep convection in the polar region (Table 2). The underlying mechanisms are presented in the subpolar region of GFDL-M and the polar region of IPSL, using the 10% annual ice coverage to delimit the two regions (Figures 8 and 9).

3.4.1. Southern Annular Mode Variability in the Subpolar Southern Ocean

In the subpolar region, the first mode of variability of FCO_2 and FO_2 in GFDL-M displays very similar patterns along the sea ice boundary (Figures 8a and 8b). This confirms that their variability is driven by the same processes. EOF1 explains $\sim 20\text{--}25\%$ of the total variance in FCO_2 and FO_2 in that region. Positive phases of the SAM ($\text{SAMI} > 0$) and enhanced winds correlate with CO_2 outgassing (negative correlation between SAMI and FCO_2) and O_2 ingassing (positive correlation between SAMI and FO_2 ; Figure 8c). Indeed, positive phases of SAM are characterized by stronger winds and enhanced upwelling of circumpolar deep waters [Love-nduski and Gruber, 2005], a process supported by the positive (negative) correlation between SAMI and wind stress (SST) in the model (Figure 8c). The vertical transport of carbon-rich and oxygen-deficient waters to the surface by the upwelling explains the enhanced outgassing of CO_2 and ingassing of O_2 . The relatively poor correlation between this mode of variability and PP suggests that ocean transport is the main driver, the contribution of biological activity being rather small or negligible (Figure 8c). The variability associated with this first mode occurs on interannual (3–4 year) and decadal (20 year) time scales (Table 2).

The six ESMs present a similar mode of variability correlated with the SAM and wind stress, supporting that SAM is a major driver of FCO_2 and FO_2 variability in this region (Table 2). This mode peaks at both interannual and decadal time scale in all ESMs except MPI-L and MPI-M, in which only the interannual component is present. While the signature of biological activity is small in GFDL-M and IPSL, it could modulate the variability related to the upwelling in CESM, GFDL-G, MPI-L, and MPI-M (significant positive correlation to FCO_2 and negative correlation to FO_2 in supporting information Figures fs03, fs04, fs07, and fs08). In particular, in CESM, the EOF analysis indicates that the variability in the Indo-Pacific sector is driven by changes in the vertical transport, while the variability in the Atlantic sector is probably driven by changes in biological activity.

3.4.2. Multidecadal Variability of Convection in the Polar Southern Ocean

The first mode of variability of FCO_2 and FO_2 in IPSL presents a very similar and localized pattern west of the Antarctic Peninsula and explains more than 40% of the variance in the polar region (Figures 9a and 9b). This mode of variability is strongly correlated with mixed layer depth (Figure 9c) and corresponds to deep convective events occurring on multidecadal time scales with major peaks at around 20 and 50–60 years (Table 2). During these events, carbon-enriched and oxygen-deficient deep waters are transported to the surface, thereby promoting CO_2 outgassing and O_2 ingassing. In addition, the transport of relatively warm deep waters to the surface prevents sea ice formation in areas of vigorous mixing and further enhances the exchange of gases across the air-sea interface.

Deep convection drives FCO_2 and FO_2 variability in the polar region in all ESMs except in CESM (Table 2). Indeed, CESM shows very little variability of FCO_2 and FO_2 and the mixed layer depth does not exceed 200 m in this region (Figures 5a1 and 5b1). The impact of this process on air-sea fluxes varies from a strong impact in GFDL-M and IPSL, in which it explains more than 30% of the fluxes variance to a much moderate impact in GFDL-G, MPI-L, and MPI-M, in which it explains $\sim 10\%$ of the variance (see supporting information Figure fs02). Deep convective events are the major forcing mechanism of the global FCO_2 and FO_2 on multidecadal time scales. The absence of such events in CESM explain why this model display such low variability on temporal scales longer than 10 years (Figures 7c and 7d). A noteworthy difference between the models is the position of the deep convection site that either develops in the Atlantic or the Pacific sector. Deep

convective events have been found previously in climate models (IPSL-L, HadGEM2-ES, and MPI-L in Royer *et al.* [2011], Séférian *et al.* [2013], and *de Lavergne et al.* [2014]). Similar events were observed from early satellite measurements, which will be discussed in more detail in section 4.

The signature of SAM and deep convection on the first EOFs is a robust feature. However, it should be noted that the variance explained by these first modes largely differ from $\sim 10\text{--}15\%$ in CESM, GFDL-G, and MPI models to $\sim 20\text{--}45\%$ in GFDL-M and IPSL (see supporting information Figure fs02). These values can appear low compared to those obtained with physical variables such as SST. However, we expect the analysis of biogeochemical fields to be more complex due to the numerous processes involved in their variability. FCO₂ and FO₂ depend on the ocean circulation, the radiative budget through SST, the wind stress through the piston velocity but also on the biological activity that is modulated by numerous parameters including nutrient (iron, nitrate, and phosphate) limitations, light availability, biological growth, mortality rates, etc. In addition, it is interesting to note that the models with lower explained variance (CESM, GFDL-G, MPI-L, and MPI-M) are the models in which biological activity is likely to impact FCO₂ and FO₂ (significant correlation to PP). In contrast, the variability in the ESMs with higher explained variance (GFDL-M and IPSL) are largely dominated by the impact of ocean circulation.

3.4.3. Modulation by the Tropical Pacific at Interannual Time Scales

The tropical Indo-Pacific significantly impacts global FCO₂ and FO₂ on interannual time scales in CESM, GFDL-G, and GFDL-M (Figures 7c and 7d). In the following, we focus on the tropical Pacific sector, where most of the variability occurs (Figure 3), and on the CESM model, in which the first two EOFs explain more than 50% of the variance (Figure 10).

The first EOF of FCO₂ and FO₂ in CESM present different patterns, strongly suggesting that the variability of FCO₂ and FO₂ is partly decoupled in this region (Figures 10a and 10c). In the upwelling regions (coastal eastern boundary and equatorial band east of 150W), the variability of FCO₂ and FO₂ are anticorrelated: the EOF1 of FCO₂ (FO₂) is positively (negatively) correlated with the Nino3.4 index and SST and negatively (positively) correlated to wind stress and mixed layer depth (Figure 10e). During positive ENSO phases (Nino3.4 > 0), the upwelling weakens (indicated by shallower mixed layer depth and thermocline) in response to weaker winds. This leads to a lower vertical input of DIC-rich and O₂-depleted waters to the surface thus favoring a relative CO₂ ingassing ($r_{FCO_2-EOF1} > 0$) and a relative O₂ outgassing ($r_{FO_2-EOF1} < 0$). Positive ENSO phases are also associated with a decrease of PP in the upwelling region, which could partly counterbalance the impact of vertical transport by decreasing FCO₂ and increasing FO₂. In addition, the O₂ concentration at the sea surface equilibrates with the atmosphere on short time scales (~ 1 month), whereas CO₂ equilibrates on much longer time scale (~ 10 month). FO₂ is therefore more likely to be modulated by rapid seasonal changes in biological uptake and vertical transports than FCO₂, which probably explains part of the decoupling between CO₂ and O₂ in this region [McKinley *et al.*, 2004].

In contrast, the first EOF of FCO₂ and FO₂ in the western Pacific positively correlates with Nino3.4 and SST, suggesting that the variability in this region is driven by solubility effects (Figures 10a, 10c, and 10e). This is confirmed by the second EOFs that shows a positive correlation between FCO₂, FO₂, and SST in the western tropical Pacific and on either side of the equatorial upwelling (Figures 10b, 10d, and 10f). Note that the patterns of the EOF2 in the eastern and central Pacific are decoupled and relatively hard to interpret in relation to ENSO. Previous studies have shown the strong imprint of other Pacific climate modes on CO₂ and O₂, such as the Pacific Decadal Oscillation [Takahashi *et al.*, 2006; Frölicher *et al.*, 2009; Valsala *et al.*, 2012; Séférian *et al.*, 2013] and the North Pacific Gyre Oscillation [Di Lorenzo *et al.*, 2008], which probably explains part of the variability in the second EOF.

As expected, ENSO is the major driver of FCO₂ and FO₂ interannual variability in the three ESMs (CESM, GFDL-G, and GFDL-M) in the tropical Pacific (Table 2). The three ESMs show similar behaviors with variations in the upwelling driving opposed variations for FCO₂ and FO₂ in the eastern and equatorial Pacific and solubility controlling analogous responses in the western Pacific and on either side of the equatorial upwelling (Figure 10 and supporting information Figures fs09 and fs10).

4. Discussion and Conclusions

In this study, we examined the internally driven natural variability of CO₂ and O₂ fluxes using control simulations in six climate models. The CO₂ and O₂ fluxes presented by this suite of models are consistent with

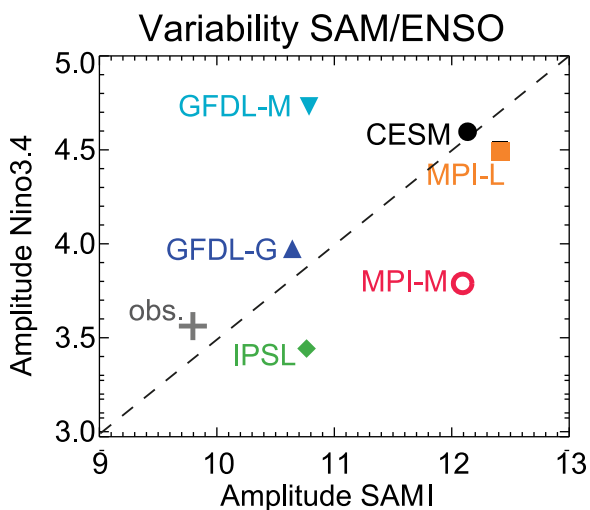


Figure 11. Relative amplitude of the (a) ENSO (in °C) and (b) SAMI (in mb) climate mode indexes in CMIP5 models and in the observations. Amplitudes are estimated as the maximum value minus the minimum value of the time series of Nino3.4 et SAMI indexes. To allow direct comparison, observed Nino3.4 (respectively SAMI) was recomputed using annual mean SST (respectively annual mean SLP) from NOAA (data available at www.esrl.noaa.gov/psd/data/climateindices/list/). The lower amplitude found for the observation is probably related to the length of the record being much smaller than the length of preindustrial simulations.

Southern Ocean, and to a lesser extent the tropical Pacific. This is in agreement with the current knowledge that interannual and low-frequency variability of carbon and oxygen are stronger in regions of intense climate modes, i.e., at high latitudes (NAO, PDO, and SAM [Emerson *et al.*, 2004; McKinley *et al.*, 2004; Takahashi *et al.*, 2006; Frölicher *et al.*, 2009; Keller *et al.*, 2012; Séférian *et al.*, 2013]) and in the tropical Pacific (ENSO [Feely *et al.*, 1999; McKinley *et al.*, 2003, 2004]). Although the variability is strong in the North Atlantic and the North Pacific, we found that the internal variability of CO₂ and O₂ fluxes at the global scale is controlled by the fluxes occurring in the Southern Ocean and the tropical Pacific region. These regions combine strong variability and sufficiently large areas to influence the global budget. The amplitude of the CO₂ and O₂ flux variations on the global scale reaches up to 6–12 Tg C yr⁻¹/40–60 Tmol O₂ yr⁻¹ on interannual time scales and 4–6 Tg C yr⁻¹/10–30 Tmol O₂ yr⁻¹ on decadal time scales. As expected, these values based on simulations of the internal variability over centuries-long simulations are lower than values of CO₂ fluxes variability derived from decades-long historical simulations including the external forcing (Anav *et al.*, 2013). In addition, note that the variability here is given independently for each frequency and should be integrated over the full spectrum to be compared to the variability derived from standard deviations.

We find that the main driver of air-sea fluxes internal variability is physical circulation and in particular vertical transport rather than changes in biological production. The six ESMs consistently display variations of CO₂ and O₂ air-sea fluxes in conjunction with SAM in the subpolar region (~40°S–55°S) and with deep convective events in the polar region (~55°S–90°S). The processes linking SAM to air-sea flux variations are relatively well known and have been described in previous model-based studies: the latitudinal shift and the change in amplitude of the zonal winds stress modulate the upwelling of carbon-rich/oxygen-depleted deep waters and hence the air-sea flux of carbon [Lenton and Matear, 2007; Lovenduski *et al.*, 2007, 2008; Verdy *et al.*, 2007; Dufour *et al.*, 2013] and oxygen [Verdy *et al.*, 2007]. Most of the variability associated with SAM occurs on interannual time scales (3–6 years) in all ESMs except the MPI models, which possess a decadal component (10–30 years). The presence of this decadal mode can however not be assessed from the temporal span of available observations.

The presence of deep convective events along the Antarctic shelf is a relatively robust feature of the ESMs considered here, CESM being the only model not reproducing these events. Satellite observations between 1974 and 1976 support the existence of such deep convective ventilation events [Carsey, 1980]. The Weddell Sea polynia, identified at that time by a giant ice-free area within the Antarctic ice pack, was characterized by deep convective overturning and a massive release of heat from the deep sea [Martinson, 1991;

climatological preindustrial flux estimates based on ocean inversions [Gruber *et al.*, 2001; Mikaloff Fletcher *et al.*, 2007]. In addition, the strong relation between the interannual variability and main climate modes of ENSO in the Pacific Ocean and SAM in the Southern Ocean is in agreement with the variability observed over the past two decades [Feely *et al.*, 2006; Ishii *et al.*, 2014; Lenton *et al.*, 2013]. We were able to identify robust mechanisms present in all climate models and behaviors that are model-specific based on centuries-long time series.

A robust feature across models are regions with highest internal variability: the North Atlantic, the North Pacific, the

Gordon, 1982; Parkinson, 1983]. Our study shows that deep convective events also promote large variations in CO₂ and O₂ air-sea fluxes. The intense vertical exchange between the surface and the abyssal ocean triggers large changes in dissolved carbon and oxygen at the surface. This effect combined with the reduction of sea-ice coverage, further enhances the gas exchange at the air-sea interface. Although this mechanism is localized in time and space, it is a major source of internal variability of air-sea fluxes on multidecadal time scales in the Southern Ocean and at the global scale. The ESMs with a strong impact of deep convection on CO₂ and O₂ air-sea exchanges are indeed the models with the highest variability on multidecadal time scales (GFDL and IPSL). In contrast, the only model not reproducing convective events shows no variability on multidecadal time scales (CESM). The presence or absence of such events reflect the difference in circulation and mean state between models. Indeed, although all CMIP5 climate models are too stratified compared with observations in the Southern Ocean, the average depth of the mixed layer and the stratification at its base widely differ [Sallée *et al.*, 2013b]. Recently, the study of *de Lavergne et al.* [2014] suggested that the absence of deep ventilation events in the past 30 years (since the polynia of 1974–1976) might be related to the enhanced stratification associated with climate change. Our study shows that these events are highly variable on decadal to multidecadal time scales and can therefore be suppressed for several decades. This natural modulation in conjunction to the stratification effect associated with climate change could further explain the suppression of any deep convective events in the last 40 years.

On interannual time scales, global CO₂ and O₂ air-sea fluxes are also modulated by the variability in the tropical Pacific. The CESM and GFDL models show a strong link between air-sea fluxes variability and ENSO, in agreement with previous results based on models and observations [Keeling *et al.*, 1989; Feely *et al.*, 1999; Chavez *et al.*, 1999; McKinley *et al.*, 2003; Peylin *et al.*, 2005; Frölicher *et al.*, 2013]. During positive phases, solubility effects lead to the outgassing of both CO₂ and O₂ in the western tropical Pacific, while the suppression of vertical transport of carbon-rich/oxygen-depleted waters leads to CO₂ ingassing and O₂ outgassing in the upwelling region along the eastern boundary and the equator. However, the tropical Pacific plays a much smaller role in the IPSL and MPI models (Figure 7). We assess the relative strength of the two interannual climate modes in these regions, ENSO and SAM, by comparing their amplitude (Figure 11). ESMs with a stronger impact of ENSO on air-sea fluxes tend to have larger Nino3.4 over SAMI amplitude ratios. Although the amplitude ratio is a simple metric that does not reflect all the processes at play in the modulation of air-sea fluxes (upwelling, biological activity, solubility, wind-driven piston velocity, etc.), this suggests that the contributions of the tropical Pacific and the Southern Ocean on interannual time scales in one given model depends on the relative strength of these two climate modes.

The variability of O₂ fluxes estimated from interannual to multidecadal time scales in this study (5–60 Tmol yr⁻¹) is of the same order of magnitude as the changes expected from climate change (~40 Tmol yr⁻¹) [Keeling *et al.*, 2010] and from external forcing by volcanic eruptions (~1 Tmol yr⁻¹) [Frölicher *et al.*, 2009]. This large internal variability in O₂ is a major limitation in the detection of long-term trends and the estimation of global ocean deoxygenation [Andrews *et al.*, 2013]. In contrast, the contribution of oceanic internal variability to global CO₂ air-sea fluxes is much lower. It is about a few percent of the uncertainty of the current ocean carbon sink estimate (2.6 ± 0.5 Pg C yr⁻¹) [Le Quéré *et al.*, 2013] and lower than the expected impact of external forcings by volcanic eruptions (2 ± 0.02 Pg C yr⁻¹) [Frölicher *et al.*, 2013]. This low contribution of internal variability to the contemporary ocean carbon budget is largely explained by the amplitude of anthropogenic CO₂ emissions, which overwhelm natural carbon exchanges [Séférian *et al.*, 2014], leading to an excess oceanic uptake of 2–3 Pg C yr⁻¹ [Le Quéré *et al.*, 2013]. In addition, perturbations due to anthropogenic activities and volcanic eruptions globally increase the CO₂ atmospheric concentration thereby strongly modifying the carbon balance, whereas regional sources of internal variability partly compensate when averaged at the global scale. Nevertheless, natural variability of internal origin can strongly affect our understanding of the carbon ocean uptake. We find that the internal variability of CO₂ air-sea fluxes can locally reach 10–20 g C m⁻² yr⁻¹, which represents 20–100% of annual mean fluxes (not shown). This strongly impacts our ability to measure and derive accurate global budgets by increasing the necessary spatiotemporal coverage to resolve the long-term trends.

Finally, although common features emerge from this multimodel study, there are still large differences between models in the strength, period and the nature of the processes driving internal variability. This should be kept in mind when examining and detecting long-term trends from a few decade-long model

results. Climate change trends are more likely to emerge from models with weaker internal variability than from models in which the strong variability partially masks long-term changes. It is however relatively difficult to assess which models represent a more realistic variability, in particular on decadal and multidecadal time scales as the temporal coverage of direct observation is limited to a few decades [Deutsch *et al.*, 2011; Stendardo and Gruber, 2012; Rödenbeck *et al.*, 2013]. Efforts are therefore needed to assess and improve the representation of interannual and decadal modes of variability. This step is essential in the perspective of applying emergent constraints [Cox *et al.*, 2013; Wenzel *et al.*, 2014] and reducing the uncertainties in future projections.

Appendix A: Identifying and Quantifying FCO₂ and FO₂ Internal Variability in CMIP5

A1. Decadal-to-Interannual Ratio

We highlight regions and models of particularly high decadal variability by computing a metric representing the decadal-to-interannual ratio, called diagnosed potential predictability (DDP) [Boer, 2004]:

$$DDP = \frac{\sigma_{20y}^2 - \frac{1}{20} * \sigma_{1y}^2}{\sigma_{1y}^2} * 100, \quad (A1)$$

where σ_{1y}^2 and σ_{20y}^2 are the variance at interannual and decadal (20 year moving average) time scales.

A2. Regional Variability and Vertical Transport

The strong contribution of vertical transport for the variability of FCO₂ and FO₂ is illustrated in Figure 5. Regions of highest variability are identified using the 80th percentile of FCO₂ and FO₂ standard deviation. The correlation between FCO₂ and FO₂ in those regions is an indicator of the contribution of solubility (positive correlation) or vertical transport and biological activity (negative correlation). To emphasize on the role of ocean circulation, we identified regions of high variability in the vertical transport, using the mean mixed layer depth (ML) and its temporal standard deviation (std(ML)). Regions of deep convection appear with ML+std(ML) > 1000 m and main regions of mode and intermediate waters formation are identified with ML+std(ML) > 200 m. In addition, regions with variable upwelling are highlighted using the standard deviation of the wind curl vertical component in areas where it is positive (std($\nabla \times \zeta$, gray contours). These metrics are not designed to accurately delimit all regions of mode water formation or upwelling, but to provide a simple description of vertical exchanges in the six ESMs.

A3. Spectral Analysis: Amplitude, Periods, and Regions Dominating the Variability

The power spectrum of a time series describes how the variance of the data is distributed over the frequency components. We used the power spectral density of the air-sea fluxes (PSD) to detect the periodicities in FCO₂ and FO₂ internal variability (supporting information Figure fs01). Significant periods of variability are identified using an autoregressive process of order 1 (AR1), i.e., significant peaks are those with an amplitude larger than the AR1 spectrum (dotted lines in Figure fs01). To further highlight the main peaks and their corresponding periodicities, we computed the amplitude of variability $V(f)$ that integrates the amount of variance lying within an interval around each frequency $f (f \pm f/10)$:

$$V(f) = 1.96 * \sqrt{\int_{f-f/10}^{f+f/10} PSD(f).df}. \quad (A2)$$

The factor 1.96 gives the amplitude of variability within the 95% confidence interval. The periods for which $V(f)$ is significant are estimated using the integrated variance expected from an AR1 spectrum ($V_{AR1}(f) = 1.96 * \sqrt{\int_{f-f/10}^{f+f/10} PSD_{AR1}(f).df}$). $V(f)$ thus allows to identify significant periods of variability in the original flux unit, i.e., Pg C/yr for FCO₂ and Tmol/yr for FO₂ (note that PSD is a variance per unit of frequency). Figure 7 presents $V(f)$ (symbol size) along with the regions that dominate the variability during each period (colors). The variance is computed separately for each region; the dominating region is the one with higher variance. Codominance occurs if the contribution of two regions differ by less than 10%.

A4. Empirical Orthogonal Functions (EOFs)

EOFs of FCO₂ and FO₂ were computed over the Southern Ocean (90°S–40°N) and tropical Pacific (20°S–20°N), the two regions dominating the global air-sea fluxes variability. The Southern Ocean was further

divided in two subregions: the subpolar and the polar regions, separated by the 10% annual sea ice coverage. We have retained the first leading principal component (PC) in the Southern Ocean and the first two PCs in the tropical Pacific that explain at least 10% of the regional air-sea fluxes total variance (see supporting information Figure fs02). The first EOF explains between 10% and 50% of FCO₂ and FO₂ total variance, which can appear low compared to those obtained with physical variables such as SST. We however expect the analysis of biogeochemical fields to be more complex due to the numerous processes involved in their variability. FCO₂ and FO₂ depends on the ocean circulation, the radiative budget through SST, the wind stress through the piston velocity but also on the biological activity that is modulated by numerous parameters including nutrient (iron, nitrate, and phosphate) limitations, light availability, biological growth, mortality rates, etc. The aim here is not to fully describe the regional variance in each ESM but to investigate the main drivers of global CO₂ and O₂ air-sea fluxes internal variability and if they are robust features across the model pool. To examine which drivers control the various modes of variability, we used linear correlations between the leading PCs and other physical and biogeochemical variables (MLD, SST, wind stress, and PP). The correlation to PP is only shown when it corresponds to a CO₂ ingassing and a O₂ outgassing, which is the impact expected from primary production. Finally, the periods at which EOFs show highest variability are determined using spectral variance. To do so, we use the same technique as described in section A3: V(f) is computed for each EOF and significant peaks are identified using the integrated variance expected from an AR1 spectrum. The identified periods are given in Table 2.

Acknowledgments

We sincerely thank R. Keeling and Y. Eddebar for the useful discussions and two anonymous reviewers for their helpful comments on the manuscript. This work was made possible, thanks to the climate modeling groups (listed in Table 1) for producing and making available their model output. We are grateful to P. Brockmann, S. Denvil, and the IPSL team for making the access to the CMIP5 database so easy. We acknowledge the World Climate Research Programme's Working Group on Coupled Modelling, which is responsible for CMIP. Support was provided by the EU FP7 project CARBOCHANGE, "Changes in carbon uptake and emissions by oceans in a changing climate," which received funding from the European Commissions Seventh Framework Programme under grant agreement 264879. For CMIP, the U.S. Department of Energy's Program for Climate Model Diagnosis and Intercomparison provides coordinating support and led development of software infrastructure in partnership with the Global Organization for Earth System Science Portals. CMIP5 data can be found at http://cmip-pcmdi.llnl.gov/cmip5/data_portal.html.

References

- Anav, A., P. Friedlingstein, M. Kidston, L. Bopp, P. Caias, P. Cox, C. Jones, M. Jung, R. Myneni, and Z. Zhu (2013), Evaluating the land and ocean components of the global carbon cycle in the cmip5 earth system models, *J. Clim.*, 26, 6801–6843, doi:10.1175/JCLI-D-12-00417.1.
- Andrews, O. D., N. L. Bindoff, P. R. Halloran, T. Ilyina, and C. Le Quéré (2013), Detecting an external influence on recent changes in oceanic oxygen using an optimal fingerprinting method, *Biogeosciences*, 10(3), 1799–1813, doi:10.5194/bg-10-1799-2013.
- Bertrand, A., M. Ballón, and A. Chaigneau (2010), Acoustic observation of living organisms reveals the upper limit of the oxygen minimum zone, *PLoS ONE*, 5, e10330, doi:10.1371/journal.pone.0010330.
- Bertrand, A., A. Chaigneau, S. Peralta, J. Ledesma, M. Graco, F. Monetti, and F. P. Chavez (2011), Oxygen: A fundamental property regulating pelagic ecosystem structure in the coastal southeastern tropical Pacific, *PLoS ONE*, 6, e29558, doi:10.1371/journal.pone.0029558.
- Boer, G. J. (2004), Long time-scale potential predictability in an ensemble of coupled climate models, *Clim. Dyn.*, 23(1), 29–44, doi:10.1007/s00382-004-0419-8.
- Bopp, L., C. L. Quéré, M. Heimann, A. C. Manning, and P. Monfray (2002), Climate-induced oceanic oxygen fluxes: Implications for the contemporary carbon budget, *Global Biogeochem. Cycles*, 16(2), 1022, doi:10.1029/2001GB001445.
- Carsey, F. D. (1980), Microwave observation of the Weddell Polynya, *Mon. Weather Rev.*, 108, 2032–2044.
- Chavez, F. P., P. G. Strutton, G. E. Friederich, R. A. Feely, G. C. Feldman, D. G. Foley, and M. J. McPhaden (1999), Biological and chemical response of the equatorial Pacific Ocean to the 1997–98 El Niño, *Science*, 286, 2126–2131.
- Cox, P. M., D. Pearson, B. B. Booth, P. Friedlingstein, C. Huntingford, C. D. Jones, and C. M. Luke (2013), Sensitivity of tropical carbon to climate change constrained by carbon dioxide variability, *Nature*, 494, 341–344, doi:10.1038/nature11882.
- de Lavergne, C., J. B. Palter, E. D. Galbraith, R. Bernardello, and I. Marinov (2014), Cessation of deep convection in the open Southern Ocean under anthropogenic climate change, *Nat. Clim. Change*, 4, 278–282, doi:10.1038/nclimate2132.
- Deutsch, C., H. Brix, T. Ito, H. Frenzel, and L. Thompson (2011), Climate-forced variability of ocean hypoxia, *Science*, 333(6040), 336–339, doi:10.1126/science.1202422.
- Di Lorenzo, E., et al. (2008), North Pacific Gyre Oscillation links ocean climate and ecosystem change, *Geophys. Res. Lett.*, 35, L08607, doi:10.1029/2007GL032838.
- Dufour, C. O., J. L. Sommer, M. Gehlen, J. C. Orr, J.-M. Molines, J. Simeon, and B. Barnier (2013), Eddy compensation and controls of the enhanced sea-to-air CO₂ flux during positive phases of the Southern Annular Mode, *Global Biogeochem. Cycles*, 27, 950–961, doi:10.1002/gbc.20090.
- Dunne, P. J., et al. (2012), GFDL's ESM2 global coupled climate-carbon Earth System Models Part I: Physical formulation and baseline simulation characteristics, *J. Clim.*, 25, 6646–6665, doi:10.1175/JCLI-D-11-00560.1.
- Emerson, S., W. Y. Watanabe, T. Ono, and S. Mecking (2004), Temporal trends in apparent oxygen utilization in the upper pycnocline of the North Pacific: 1980–2000, *J. Oceanogr.*, 60(1), 139–147.
- Fay, A. R., and G. A. McKinley (2013), Global trends in surface ocean pCO₂ from in situ data, *Global Biogeochem. Cycles*, 27, 541–557, doi:10.1002/gbc.20051.
- Feely, R. A., R. Wanninkhof, T. Takahashi, and P. Tans (1999), Influence of El Niño on the equatorial Pacific contribution to atmospheric CO₂ accumulation, *Nature*, 398, 597–601, doi:10.1038/19273.
- Feely, R. A., T. Takahashi, R. Wanninkhof, M. J. McPhaden, C. E. Cosca, S. C. Sutherland, and M.-E. Carr (2006), Decadal variability of the air-sea CO₂ fluxes in the equatorial Pacific Ocean, *J. Geophys. Res.*, 111, C08S90, doi:10.1029/2005JC003129.
- Frölicher, T. L., F. Joos, G.-K. Plattner, M. Steinacher, and S. C. Doney (2009), Natural variability and anthropogenic trends in oceanic oxygen in a coupled carbon cycle-climate model ensemble, *Global Biogeochem. Cycles*, 23, GB1003, doi:10.1029/2008GB003316.
- Frölicher, T. L., F. Joos, C. C. Raible, and J. L. Sarmiento (2013), Atmospheric CO₂ response to volcanic eruptions: The role of ENSO, season, and variability, *Global Biogeochem. Cycles*, 27, 239–251, doi:10.1002/gbc.20028.
- Garcia, H. E., and R. F. Keeling (2001), On the global oxygen anomaly and air-sea flux, *J. Geophys. Res.*, 106(C12), 31,155–31,166, doi:10.1029/1999JC000200.
- Gent, R. P., et al. (2011), The community climate system model version 4, *J. Clim.*, 24, 4973–4991.

- Gerber, M., and F. Joos (2010), Carbon sources and sinks from an ensemble Kalman filter ocean data assimilation, *Global Biogeochem. Cycles*, 24, GB3004, doi:10.1029/2009GB003531.
- Gerber, M., F. Joos, M. Vzquez-Rodrguez, F. Touratier, and C. Goyet (2009), Regional air-sea fluxes of anthropogenic carbon inferred with an ensemble Kalman filter, *Global Biogeochem. Cycles*, 23, GB1013, doi:10.1029/2008GB003247.
- Giorgetta, M. A., et al. (2013), Climate and carbon cycle changes from 1850 to 2100 in MPI-ESM simulations for the coupled model inter-comparison project phase 5, *J. Adv. Model. Earth Syst.*, 5, 572–597, doi:10.1002/jame.20038.
- Gordon, A. L. (1982), Weddell deep water variability, *J. Mar. Res.*, 40, 199–217.
- Gruber, N., M. Glooer, S.-M. Fan, and J. L. Sarmiento (2001), Air-sea flux of oxygen estimated from bulk data: Implications for the marine and atmospheric oxygen cycles, *Global Biogeochem. Cycles*, 15(4), 783–803, doi:10.1029/2000GB001302.
- Helm, P. K., N. L. Bindoff, and J. A. Church (2011), Observed decreases in oxygen content of the global ocean, *Geophys. Res. Lett.*, 38, L23602, doi:10.1029/2011GL049513.
- Ishii, M., et al. (2014), Air-sea CO₂ flux in the Pacific Ocean for the period 1990–2009, *Biogeosciences*, 11, 709–734, doi:10.5194/bg-11-709-2014.
- Jacobson, A. R., S. E. Mikaloff Fletcher, N. Gruber, J. L. Sarmiento, and M. Glooer (2007), A joint atmosphere-ocean inversion for surface fluxes of carbon dioxide: 2. Regional results, *Global Biogeochem. Cycles*, 21, GB1020, doi:10.1029/2006GB002703.
- Keeling, C. D., R. B. Bacastow, A. F. Carter, S. C. Piper, T. P. Whorf, M. Heimann, W. G. Mook, and H. Roeloffzen (1989), A three-dimensional model of atmospheric CO₂ transport based on observed winds: 1. Analysis of observational data, in *Aspects of Climate Variability in the Pacific and the Western Americas*, edited by D. H. Peterson, pp. 165–236, AGU, Washington, D. C., doi:10.1029/GM055p0165.
- Keeling, R., and A. Manning (2014), Studies of recent changes in atmospheric O₂ content, in *Treatise on Geochemistry*, 2nd ed., edited by H. D. Holland and K. K. Turekian, pp. 385–404, Elsevier, Oxford, U. K., doi:10.1016/B978-0-08-095975-7.00420-4.
- Keeling, R. F., A. Körtzinger, and N. Gruber (2010), Ocean deoxygenation in a warming world, *Annu. Rev. Mar. Sci.*, 2(1), 199–229, doi:10.1146/annurev.marine.010908.163855.
- Keller, K., et al. (2012), Variability of the ocean carbon cycle in response to the north Atlantic oscillation, *Tellus, Ser. B*, 2012, 64, 18738, doi:10.3402/tellusb.v64i0.18738.
- Keller, K. M., F. Joos, and C. C. Raible (2014), Time of emergence of trends in ocean biogeochemistry, *Biogeosciences*, 11(13), 3647–3659, doi:10.5194/bg-11-3647-2014.
- Khatiwala, S., F. Primeau, and T. Hall (2009), Reconstruction of the history of anthropogenic CO₂ concentrations in the ocean, *Nature*, 462, 346–349, doi:10.1038/nature08526.
- Khatiwala, S., et al. (2013), Global ocean storage of anthropogenic carbon, *Biogeosciences*, 10(4), 2169–2191, doi:10.5194/bg-10-2169-2013.
- Kouketsu, S., and A. M. Murata (2014), Detecting decadal-scale increases in anthropogenic CO₂ in the ocean, *Geophys. Res. Lett.*, 41, 4594–4600, doi:10.1002/2014GL060516.
- Landschützer, P., N. Gruber, D. C. E. Bakker, U. Schuster, S. Nakaoka, M. R. Payne, T. P. Sasse, and J. Zeng (2013), A neural network-based estimate of the seasonal to inter-annual variability of the Atlantic Ocean carbon sink, *Biogeosciences*, 10, 7793–7815, doi:10.5194/bg-10-7793-2013.
- Le Quéré, C., et al. (2007), Saturation of the Southern Ocean CO₂ sink due to recent climate change, *Science*, 316, 1735–1738, doi:10.1126/science.1136188.
- Le Quéré, C., et al. (2013), Global carbon budget 2013, *Earth Syst. Sci. Data Discuss.*, 6(2), 689–760, doi:10.5194/essdd-6-689-2013.
- Lenton, A., and R. J. Matear (2007), Role of the southern annular mode (SAM) in Southern Ocean CO₂ uptake, *Global Biogeochem. Cycles*, 21, GB2016, doi:10.1029/2006GB002714.
- Lenton, A., et al. (2013), Sea-air CO₂ fluxes in the Southern Ocean for the period 1990–2009, *Biogeosciences*, 10(6), 4037–4054, doi:10.5194/bg-10-4037-2013.
- Lovenduski, N. S., and N. Gruber (2005), Impact of the southern annular mode on southern ocean circulation and biology, *Geophys. Res. Lett.*, 32, L11603, doi:10.1029/2005GL022727.
- Lovenduski, N. S., N. Gruber, S. C. Doney, and I. D. Lima (2007), Enhanced CO₂ outgassing in the Southern Ocean from a positive phase of the Southern Annular Mode, *Global Biogeochem. Cycles*, 21, GB2026, doi:10.1029/2006GB002900.
- Lovenduski, N. S., N. Gruber, and S. C. Doney (2008), Toward a mechanistic understanding of the decadal trends in the Southern Ocean carbon sink, *Global Biogeochem. Cycles*, 22, GB3016, doi:10.1029/2007GB003139.
- Majkut, D. J., B. R. Carter, T. L. Frölicher, C. O. Dufour, K. B. Rodgers, and J. L. Sarmiento (2014), An observing system simulation for Southern Ocean carbon dioxide uptake, *Philos. Trans. R. Soc. A*, 372, 2009–2025, doi:10.1098/rsta.2013.0046.
- Martinson, D. (1991), Open ocean convection in the Southern Ocean, in *Deep Convection and Deep Water Formation in the Oceans Proceedings of the International Monterey Colloquium on Deep Convection and Deep Water Formation in the Oceans*, Elsevier Oceanogr. Ser., vol. 57, edited by P. Chu and J. Gascard, pp. 37–52, Elsevier Sci. Publ., Amsterdam, doi:10.1016/S0422-9894(08)70059-X.
- Matear, R. J., and A. C. Hirst (2003), Long-term changes in dissolved oxygen concentrations in the ocean caused by protracted global warming, *Global Biogeochem. Cycles*, 17(4), 1125, doi:10.1029/2002GB001997.
- Matear, R. J., A. C. Hirst, and B. I. McNeil (2000), Changes in dissolved oxygen in the Southern Ocean with climate change, *Geochim. Geophys. Geosyst.*, 1(11), 1050, doi:10.1029/2000GC000086.
- McKinley, G. A., M. J. Follows, J. Marshall, and S.-M. Fan (2003), Interannual variability of air-sea O₂ fluxes and the determination of CO₂ sinks using atmospheric O₂/N₂, *Geophys. Res. Lett.*, 30(3), 1101, doi:10.1029/2002GL016044.
- McKinley, G. A., M. J. Follows, and J. Marshall (2004), Mechanisms of air-sea CO₂ flux variability in the equatorial Pacific and the North Atlantic, *Global Biogeochem. Cycles*, 18, GB2011, doi:10.1029/2003GB002179.
- McKinley, G. A., A. R. Fay, T. Takahashi, and N. Metzl (2011), Convergence of atmospheric and North Atlantic carbon dioxide trends on multi-decadal timescales, *Nat. Geosci.*, 4, 1–5, doi:10.1038/ngeo1193.
- Mikaloff Fletcher, S. E., et al. (2006), Inverse estimates of anthropogenic CO₂ uptake, transport, and storage by the ocean, *Global Biogeochem. Cycles*, 20, GB2002, doi:10.1029/2005GB002530.
- Mikaloff Fletcher, S. E., et al. (2007), Inverse estimates of the oceanic sources and sinks of natural CO₂ and the implied oceanic carbon transport, *Global Biogeochem. Cycles*, 21, GB1010, doi:10.1029/2006GB002751.
- Najjar, R. G., and R. F. Keeling (2000), Mean annual cycle of the air-sea oxygen flux: A global view, *Global Biogeochem. Cycles*, 14(2), 573–584, doi:10.1029/1999GB900086.
- Nan, S., and J. Li (2003), The relationship between the summer precipitation in the Yangtze River valley and the boreal spring Southern Hemisphere annular mode, *Geophys. Res. Lett.*, 30(24), 2266, doi:10.1029/2003GL018381.
- Orr, C. J., et al. (2005), Anthropogenic ocean acidification over the twenty-first century and its impact on calcifying organisms, *Nature*, 437, 681–686, doi:10.1038/nature04095.

- Parkinson, C. L. (1983), On the development and cause of the Weddell Polynya in a sea ice simulation, *J. Phys. Oceanogr.*, **13**, 501–511, doi: 10.1175/1520-0485(1983)013.
- Peylin, P., P. Bousquet, C. Le Quéré, S. Sitch, P. Friedlingstein, G. McKinley, N. Gruber, P. Rayner, and P. Ciais (2005), Multiple constraints on regional CO₂ flux variations over land and oceans, *Global Biogeochem. Cycles*, **19**, GB1011, doi:10.1029/2003GB002214.
- Plattner, G.-K., F. Joos, and T. F. Stocker (2002), Revision of the global carbon budget due to changing air-sea oxygen fluxes, *Global Biogeochem. Cycles*, **16**(4), 1096, doi:10.1029/2001GB001746.
- Pörtner, O. H. (2008), Ecosystem effects of ocean acidification in times of ocean warming: A physiologists view, *Mar. Ecol. Prog. Ser.*, **373**, 203–217.
- Prince, E. D., and C. P. Goodey (2006), Hypoxia-based habitat compression of tropical pelagic fishes, *Fish. Oceanogr.*, **15**, 451–464.
- Rödenbeck, C., R. F. Keeling, D. C. E. Bakker, N. Metzl, A. Olsen, C. Sabine, and M. Heimann (2013), Global surface-ocean pCO₂ and sea-air CO₂ flux variability from an observation-driven ocean mixed-layer scheme, *Ocean Sci.*, **9**(2), 193–216, doi:10.5194/os-9-193-2013.
- Royer, T. C., et al. (2011), Regional impacts of climate change and atmospheric CO₂ on future ocean carbon uptake: A multimodel linear feedback analysis, *J. Clim.*, **24**, 2300–2318, doi:10.1175/2010JCLI3787.1.
- Sabine, C. L., et al. (2004), The oceanic sink for anthropogenic CO₂, *Science*, **305**, 367–371, doi:10.1126/science.1097403.
- Sallée, J.-B., E. Shuckburgh, N. Bruneau, A. J. S. Meijers, T. J. Bracegirdle, Z. Wang, and T. Roy (2013a), Assessment of Southern Ocean water mass circulation and characteristics in CMIP5 models: Historical bias and forcing response, *J. Geophys. Res. Oceans*, **118**, 1830–1844, doi: 10.1002/jgrc.20135.
- Sallée, J.-B., E. Shuckburgh, N. Bruneau, A. J. S. Meijers, T. J. Bracegirdle, and Z. Wang (2013b), Assessment of Southern Ocean mixed-layer depths in CMIP5 models: Historical bias and forcing response, *J. Geophys. Res. Oceans*, **118**, 1845–1862, doi:10.1002/jgrc.20157.
- Schuster, U., A. Watson, N. Bates, A. Corbiere, M. Gonzalez-Davila, N. Metzl, D. Pierrot, and M. Santana-Casiano (2009), Trends in North Atlantic sea-surface fCO₂ from 1990 to 2006, *Deep Sea Res., Part II*, **56**(8–10), 620–629, doi:10.1016/j.dsr2.2008.12.011.
- Séférian, R., D. Iudicone, L. Bopp, T. Roy, and G. Madec (2012), Water mass analysis of effect of climate change on air-sea CO₂ fluxes: The Southern Ocean, *J. Clim.*, **25**, 3894–3908, doi:10.1175/JCLI-D-11-00291.1.
- Séférian, R., L. Bopp, D. Swingedouw, and J. Servonnat (2013), Dynamical and biogeochemical control on the decadal variability of ocean carbon fluxes, *Earth Syst. Dyn.*, **4**, 109–127, doi:10.5194/esd-4-109-2013.
- Séférian, R., A. Ribes, and L. Bopp (2014), Detecting the anthropogenic influences on recent changes in ocean carbon uptake, *Geophys. Res. Lett.*, **41**, 5968–5977, doi:10.1002/2014GL061223.
- Stendardo, I., and N. Gruber (2012), Oxygen trends over five decades in the North Atlantic, *J. Geophys. Res.*, **117**, C11004, doi:10.1029/2012JC007909.
- Stramma, L., E. D. Prince, S. Schmidtko, J. Luo, J. P. Hoolihan, M. Visbeck, D. W. R. Wallace, P. Brandt, and A. Körtzinger (2011), Expansion of oxygen minimum zones may reduce available habitat for tropical pelagic fishes, *Nat. Clim. Change*, **2**, 33–37, doi:10.1038/nclimate1304.
- Takahashi, T., et al. (2002), Global sea-air CO₂ flux based on climatological surface ocean pCO₂, and seasonal biological and temperature effects, *Deep Sea Res., Part II*, **49**(9–10), 1601–1622, doi:10.1016/S0967-0645(02)00003-6.
- Takahashi, T., S. C. Sutherland, R. A. Feely, and R. Wanninkhof (2006), Decadal change of the surface water pCO₂ in the north pacific: A synthesis of 35 years of observations, *J. Geophys. Res.*, **111**, C07S05, doi:10.1029/2005JC003074.
- Takahashi, T., et al. (2009), Climatological mean and decadal change in surface ocean pCO₂, and net sea-air CO₂ flux over the global oceans, *Deep Sea Res., Part II*, **56**(8–10), 554–577, doi:10.1016/j.dsr2.2008.12.009.
- Taylor, E. K., R. J. Stouffer, and G. A. Meehl (2012), An overview of CMIP5 and the experiment design, *Bull. Am. Meteorol. Soc.*, **99**, 485–498, doi:10.1175/BAMS-D-11-00094.1.
- Tjiputra, J., A. Olsen, L. Bopp, A. Lenten, B. Pfeil, T. Roy, J. Segschneider, I. Totterdell, and C. Heinze (2014), Long-term surface pCO₂ trends from observations and models, *Tellus, Ser. B*, **2014**, 66, 23083, doi:10.3402/tellusb.v66.23083.
- Valsala, V., S. Maksyutov, M. Telszewski, S. Nakaoaka, Y. Nojiri, M. Ikeda, and R. Murtugudde (2012), Climate impacts on the structures of the North Pacific air-sea CO₂ flux variability, *Biogeosciences*, **9**(1), 477–492, doi:10.5194/bg-9-477-2012.
- Verdy, A., S. Dutkiewicz, M. J. Follows, J. Marshall, and A. Czaja (2007), Carbon dioxide and oxygen fluxes in the Southern Ocean: Mechanisms of interannual variability, *Global Biogeochem. Cycles*, **21**, GB2020, doi:10.1029/2006GB002916.
- Wenzel, S., P. M. Cox, V. Eyring, and P. Friedlingstein (2014), Emergent constraints on climate-carbon cycle feedbacks in the CMIP5 Earth system models, *J. Geophys. Res. Biogeosciences*, **119**, 794–807, doi:10.1002/2013JG002591.